SEARCH FOR $t\bar{t}Z' \to t\bar{t}t\bar{t}$ PRODUCTION IN THE MULTILEPTON FINAL STATE IN pp COLLISIONS AT $\sqrt{s} = 13$ TEV WITH THE ATLAS DETECTOR

By

Hieu Le

A DISSERTATION

Submitted to
Michigan State University
in partial fulfillment of the requirements
for the degree of

Physics — Doctor of Philosophy

2025

ABSTRACT

Lorem ipsum dolor sit amet, consectetur adipiscing elit, sed do eiusmod tempor incididunt ut labore et dolore magna aliqua. Ut enim ad minim veniam, quis nostrud exercitation ullamco laboris nisi ut aliquip ex ea commodo consequat. Duis aute irure dolor in reprehenderit in voluptate velit esse cillum dolore eu fugiat nulla pariatur. Excepteur sint occaecat cupidatat non proident, sunt in culpa qui officia deserunt mollit anim id est laborum.

ACKNOWLEDGMENTS

Advisor: Reinhard Schwienhorst

Postdoc: Binbin Dong

Committee

MSU group

ATLAS analysis group

Friend: Daniel, Grayson, Bella, Eric, Jordan

Other friends: Jasper, Adam, Brittany

Parents

Spouse: Allen Sechrist

ATLAS in general & funding agencies

PREFACE

This is my preface. remarks remarks remarks

TABLE OF CONTENTS

List of Tables

List of Figures

KEY TO ABBREVIATIONS

Physical & Mathematical Quantities

χ^2 chi-squared

d_0 transverse impact parameter

ΔR angular distance

$\sqrt{s}$ center-of-mass energy

η pseudorapidity

E_T transverse energy

$E_\mathrm{T}^\mathrm{miss}$ missing transverse energy

Γ decay width

γ_5 chirality projection operator

γ_μ Dirac matrices

H_0 null hypothesis

H_T scalar sum of transverse momenta p_T of all objects in an event

$\mathcal{L}$ Lagrangian

$\mathcal{L}(\theta)$ likelihood function

L instantaneous luminosity

$m_{\ell\ell}$ dilepton invariant mass

μ signal strength

μ_F factorization scale

μ_R renormalization scale

N_jets number of jets/jet multiplicity

$\mathcal{O}(n)$ on the order of n

$\mathcal{P}$ Poisson probability

p_T transverse momentum

189   Q electric charge

190   q_μ profile likelihood ratio

191   σ standard deviation

192   $\sigma[\text{b}]$ cross-section

193   z_0 longitudinal impact parameter

Particles & Processes

195   γ^* virtual photon

196   gg gluon-gluon fusion

197   pp proton-proton

198   PbPb   lead-lead

199   q quark

200   $q\bar{q}$ quark-antiquark pair

201   $t\bar{t}$ top/anti-top quark pair

202   $t\bar{t}$ top pair in association with another particle

203   $t\bar{t}t\bar{t}$ four-top-quark

204   V massive vector bosons ($W^\pm$, Z)

205   H Higgs in association with a vector boson

Acronyms

207   **1LOS**   one lepton, or two leptons of opposite charges

208   **AF3**   AtlFast3 fast simulation

209   **ALICE**   A Large Ion Collider Experiment

210   **ATLAS**   A Toroidal LHC ApparatuS

211   **AWAKE**   Advanced WAKEfield Experiment

212   **BDT**   boosted decision tree

213   **BR**   branching ratio

214   **BSM**   Beyond the Standard Model

215 **CB** combined muon

216 **CERN** European Organization for Nuclear Research

217 **CKM** Cabibbo-Kobayashi-Maskawa matrix

218 **CL** confidence level

219 **CMS** Compact Muon Solenoid

220 **CP** charge-parity symmetry

221 **CR** control region

222 **CSC** Cathode Strip Chambers

223 **CTP** Central Trigger Processor

224 **ECIDS** Electron Charge ID Selector

225 **EM** electromagnetic

226 **EW** electroweak

227 **FASER** ForwArd Search ExpeRiment

228 **FCal** forward calorimeter

229 **FS** full detector simulation

230 **GNN** graph neural network

231 **GRL** Good Run List

232 **GSC** Global Sequential Calibration

233 **GSF** Gaussian-sum filter

234 **GUT** Grand Unified Theory

235 **HEC** hadronic endcap calorimeter

236 **HF** heavy-flavor

237 **HL-LHC** High-Luminosity Large Hadron Collider

238 **HLT** High-Level Trigger

239 **ID** Inner Detector

240 **IP** interaction point

241 **JER** jet energy resolution

242 **JES** jet energy scale

243 **JVT** Jet Vertex Tagger

244 **KATRIN** Karlsruhe Tritium Neutrino Experiment

245 **L1** Level 1

246 **LAr** liquid argon

247 **LF** light-flavor

248 **LH** likelihood

249 **LHC** Large Hadron Collider

250 **LHCb** Large Hadron Collider beauty

251 **LINAC** linear accelerator

252 **LLH** log-likelihood

253 **LO** leading order

254 **MC** Monte Carlo simulation

255 **ME** matrix element

256 **ML** multilepton

257 **MS** Muon Spectrometer

258 **MDT** Monitored Drift Tubes

259 **MET** missing transverse energy

260 **NF** normalization factor

261 **NNJvt** Neural Network-based Jet Vertex Tagger

262 **NLO** next-to-leading order

263 **NNLO** next-to-next-to-leading order

264 **NP** nuisance parameter

265 **OP** operating point (also working point)

266 **OS** opposite-sign

267 **PCBT** pseudo-continuous b-tagging

268 **PDF** parton distribution function

269 **POI** parameter of interest

270 **PS** parton shower

271 **PV** primary vertex

272 **QCD** quantum chromodynamics

273 **QED** quantum electrodynamics

274 **QFT** quantum field theory

275 **QmisID** charge mis-identification

276 **RPC** Resistive Plate Chamber

277 **SCT** Semiconductor Tracker

278 **SF** scale factor

279 **SM** Standard Model

280 **SR** signal region

281 **SS** same-sign

282 **SSB** spontaneous symmetry breaking

283 **SS2L** same-sign dilepton

284 **SSML** same-sign dilepton, or more than two leptons of any charges

285 **TDAQ** Trigger and Data Acquisition

286 **TGC** Thin-Gap Chamber

287 **TRT** Transition Radiation Tracker

288 **VEV** vacuum expectation value

289 **VR** validation region

290 **UE** underlying-event

Chapter 1. Introduction

The 20$^{\text{th}}$ century ushered in a revolutionary period for mankind's understanding of the fundamental nature of matter and the forces that govern our universe with the development of special relativity and quantum mechanics, which redefined our understanding of space, time, energy and matter at the furthest extremes of scale from the vast reaches of the cosmos to the tiniest constituents of matter. Building on these principles, Quantum Electrodynamics (QED) (citation) was developed as the first successful quantum field theory (QFT) describing electromagnetism. The discovery of beta decay (citation) and its paradoxical behaviors within the framework of QED prompted the prediction of neutrinos and development of the theory of weak interaction.

At around the same time, a spectrum of strongly interacting particles was discovered (citation) as particle accelerators probed deeper into atomic nuclei, leading to the formation of the quark model in the 1960s (citation) and with it a hypothesized new binding force, the strong force. However, the QFT framework remained incapable of describing the weak and strong interactions until advancements in gauge theory and the incorporation of non-Abelian gauge theory into QFT resulted in the formation of Yang-Mills theory [1, 2]. This sparked a renaissance in modern physics with the unification of electromagnetism and weak force in 1967 (citation) under the framework of electroweak (EW) theory, as well as the development of Quantum Chromodynamics (QCD) (citation) to describe the strong force binding quarks.

At this point, the prediction of massless bosons within EW formalism remained a contradiction to the predicted massive $W^{\pm}$ and Z bosons that mediate the weak force. This was resolved by the introduction of EW spontaneous symmetry breaking and the Higgs mechanism in 1964 [3–5], which explained the generation of masses for both the EW bosons

1

and fermions. Together, these developments culminated in the Standard Model of particle physics SM (citation), a comprehensive theory that described the electromagnetic, weak, and strong interactions, classified all known fundamental particles and predicted mathematically consistent but not yet observed particles. Following its inception, particles predicted by the Standard Model were gradually observed experimentally, starting with the gluon in 1979 (citation), then the W and Z bosons (citation), and finally the top quark in 1995 (citation). The final missing piece was confirmed as the Higgs boson was observed in 2012 independently by the ATLAS [6] and CMS [7] detectors at the Large Hadron Collider, completing the Standard Model after a 40-year search and cementing it as the most successful framework so far describing fundamental constituents of matter and their governing forces.

Despite its successes, the Standard Model remains incomplete. Key unanswered questions include the nature of dark matter (citation), which makes up about 27% of the universes energy content but has no explanation within the Standard Model; the origin of neutrino masses and their oscillations (citation); the observed matter-antimatter asymmetry in the universe (citation); possible unification of the EW and strong interaction into a Grand Unified Theory (GUT) (citation); and the hierarchy problem (citation) describing the large discrepancy in scales between forces and the apparent lightness of the Higgs boson compared to values predicted from quantum corrections.

After the discovery of the Higgs boson, efforts have been underway to construct new hypotheses and models in search of beyond the Standard Model (BSM) physics via different avenues, one of which being direct searches at colliders for new resonances or particles not predicted by the SM. In particular, the top quark possesses large mass and strong coupling to the Higgs boson [8] which gives it a special role in many proposed BSM models as a possible connection with strong coupling to new particles and heavy resonances. In addition, top

quark has a clean decay signature with well-understood final states and is produced in abundance at the LHC from pp collisions in the form of top pairs $t\bar{t}$ (citation). This dissertation presents a search for the production of a heavy resonance that couple preferentially to top quark (top-philic) in association with a top pair $(t\bar{t})$ in the final state with either two leptons of the same electric charge or at least three leptons (SSML). The search is performed using the four-top $(t\bar{t}t\bar{t})$ production channel, assuming the hypothesized top-philic heavy resonance decays predominantly to $t\bar{t}$.

A similar search for top-philic heavy resonances was performed using a $t\bar{t}t\bar{t}$ final state containing either one lepton or two opposite-sign leptons (1LOS) [9] with a much larger branching ratio of 56%, compared to SSML at 12%. Despite the small cross-section within the SM, the $t\bar{t}t\bar{t}$ SSML final state provides heightened sensitivity to BSM physics and higher signal-to-background ratio than inclusive resonance searches (e.g. in dijet or dilepton final states) due to the distinctive signal signature and suppression of large SM background processes in $t\bar{t} + X$ production (citation). Additionally, cross-section for $t\bar{t}t\bar{t}$ production can be enhanced by many proposed BSM models including see-saw mechanism (citation), supersymmetry (SUSY) (citation), Effective Field Theory (EFT) operators (citation), vector-like quarks (citation) and two-Higgs-doublet models (2HDM) (citation). Searching within this channel is particularly motivated by the recent observed excess in measurement of four-top production in the SSML final state at the LHC by the ATLAS detector [10] with a measured cross-section of 24^{+7}_{-6} fb, almost double the SM prediction of $13.4^{+1.0}_{-1.8}$ fb.

The search attempts to reconstruct the top-philic resonance directly to search for new physics with minimal dependency on the model choice. In addition, a simplified color-singlet vector boson model [11] is employed for model-dependent interpretations, including setting exclusion limits on the production cross-section and model parameters. Data-driven

background estimation methods are implemented for $t\bar{t}W$ and charge misidentification back-ground to rectify mismodeling related to jet multiplicity in simulated background that were not covered in the previous 1LOS search [9]. These methods were employed similarly to great effects in SM $t\bar{t}t\bar{t}$ analyses [10, 12].

This dissertation is organized as follows. Chapter 2 presents the formalism of the SM and relevant BSM concepts. Chapter 3 provides an introduction to the LHC and ATLAS detector. Chapter 4 describes the reconstruction and identification of physics object from detector signals. Chapter 5 defines the data and simulated samples used in the analysis. Chapter 6 describes the analysis strategy, including object definition, analysis region description and background estimation methods. Chapter 7 summarizes the uncertainties involved in the analysis. Chapter 8 presents the statistical interpretation and analysis results. Finally, chapter 9 discusses a summary of the analysis and future outlook.

Chapter 2. Theoretical Overview

2.1 The Standard Model

The Standard Model of Physics (SM) [13] is currently the most successful formalism to describe the physical world at a microscopic scale by providing descriptions for all currently known elementary particles, along with three out of four fundamental forces (electromagnetism, weak force, strong force) with the exception of gravity. The SM is however not perfect, and there remains unanswered questions that require development and discovery of new physics beyond the Standard Model (BSM). This chapter describes an overview of important components within the SM and relevant BSM aspects for this analysis.

2.1.1 Elementary particles

Elementary particles in the SM can be classified into two groups: bosons consisting of particles following Bose-Einstein statistics with integer spin, and fermions consisting of particles following Fermi-Dirac statistics with half-integer spin. Fermions are the building blocks of composite particles and consequently all known matter, and can be further classified into quarks & leptons. Bosons act as force mediators for all fundamental forces described by the SM, and can either be a scalar boson with spin 0 or vector gauge bosons with spin 1. For each elementary particle, there also exists a corresponding antiparticle with identical mass and opposite charge (electric or color). Figure 2.1 shows all known elementary particles in the SM.

Figure content:

2.3 MeV R/G/B 2/3	1.28 GeV R/G/B 2/3	173.2 GeV R/G/B 2/3	← charge ← colors ← mass
u	c	t	← spin
up 1/2	charm 1/2	top 1/2	

125.1 GeV
H
Higgs 0

4.8 MeV R/G/B -1/3	95 MeV R/G/B -1/3	4.7 GeV R/G/B -1/3	
d	s	b	g
down 1/2	strange 1/2	bottom 1/2	gluon 1

511 keV -1	105.7 MeV -1	1.777 GeV -1	
e	μ	τ	γ
electron 1/2	muon 1/2	tau 1/2	photon 1

< 2 eV	< 190 keV	< 18.2 MeV	80.4 GeV ±1	91.2 GeV
ν_e	ν_μ	ν_τ	$W^\pm$	Z
e neutrino 1/2	μ neutrino 1/2	τ neutrino 1/2	1	1

graviton

6 quarks (+6 anti-quarks)
6 leptons (+6 anti-leptons)

strong nuclear force (color)
electromagnetic force (charge)
weak nuclear force (weak isospin)
gravitational force (mass)

12 fermions (+12 anti-fermions) increasing mass →
5 bosons (+1 opposite charge W)

Figure 2.1: Particles within the SM and their properties [14].

Fermions

Fermions consist of quarks and leptons with six flavors each, grouped into three generations of doublets. The six quark flavors are up (u), down (d), charm (c), strange (s), bottom (b) and top (t), arranged in increasing order of mass. The quark flavors form three doublets (u, d), (c, s) and (t, b), with each doublet containing one quark with electric charge of $+2/3$ (u, s, t), and the other with charge of $-1/3$ (d, c, b). Each quark also possesses a property known as color charge, with possible values of red (R), green (G), blue (B) or their corresponding anticolor $(\bar{R}, \bar{G}, \bar{B})$. Color charge follows color confinement rules, which allows only configurations of quarks with total neutral color charge to exist in isolation. Neutral

charge configurations can be formed from either a set of three colors (R, G, B), a set of a color and its anticolor, or any combination of the two. Consequently, quarks can only exist in bound states called hadrons and no isolated quark can be found in a vacuum. Quarks are the only elementary particles in the SM that can interact with all four fundamental forces.

The three leptons doublets consist of three charged leptons: electron (e), muon (μ), tau (τ), and their respective neutrino flavors: electron neutrino (ν_e), muon neutrino (ν_μ), tau neutrino (ν_τ). Charged leptons carry an electric charge of -1, while their antiparticles carry the opposite charge $(+1)$ and their corresponding neutrino flavors carry no charge. Charged leptons interact with all fundamental forces except the strong force, while neutrinos only interact with the weak force and gravity.

Bosons

The SM classifies bosons into two types: one scalar boson with spin 0 known as the Higgs (H) boson, and vector gauge bosons with spin 1 known as gluons (g), photon (γ), $W^\pm$ and Z bosons. Gluons and photon are massless, while the $W^\pm$, Z and H bosons are massive. Each vector gauge boson serves as the mediator for a fundamental force described by the SM. Gluons are massless particles mediating the strong interaction by carrying color charges between quarks following quantum chromodynamics (QCD). Each gluon carries a non-neutral color charge out of eight linearly independent color states in the gluon color octet [15]. Photon is the massless and charge-neutral mediator particle for the electromagnetic interaction following quantum electrodynamics (QED). The $W^\pm$ and Z bosons are massive mediator particles for the weak interaction, with the $W^\pm$ boson carrying an electric charge of ± 1 while the Z boson is charge neutral.

Other than the vector gauge boson, the only scalar boson in the SM is the massive and

charge neutral Higgs boson. The Higgs boson does not mediate any fundamental force like vector bosons, but serve to provide the rest mass for all massive elementary particles in the SM through the Higgs mechanism described in section 2.1.2.3.

Top quark

As of now, the top quark (t) is the heaviest particle in the SM with mass of about 173 GeV [16], approaching the EW symmetry breaking scale. Its high mass gives the top quark the strongest Yukawa coupling to the Higgs boson ($y_t \approx 1$) [8] and exotic resonances in many proposed BSM models [17–20], making the top quark and its processes attractive vehicles with which to probe new physics.

Due to its mass, the top quark has a very short lifetime of 10^{-24} s [16] and decays before it can hadronize following color confinement. The top quark decays to a W boson and a b-quark with a branching ratio of almost 100%. The W boson can subsequently decay hadronically or leptonically (Figure 2.2), with branching ratios of approximately 68% and 32% respectively. All lepton flavors have similar branching ratios during a leptonic W decay, assuming lepton universality.
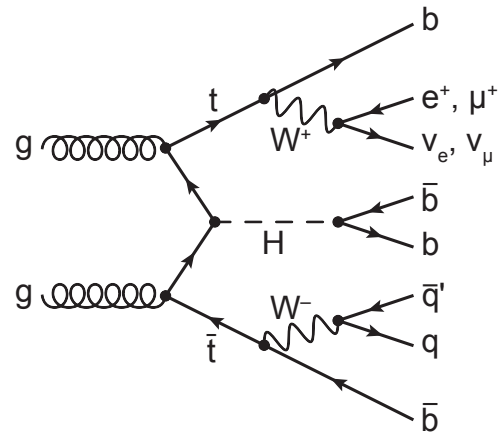
Figure 2.2: Feynman diagram for $t\bar{t}$ production and subsequent decay processes [21]. Top quark decays into a W-boson and b-quark, and W-boson can decay to a $q\bar{q}$ or a $\ell\nu_\ell$ pair.

additional section on 4top production?

2.1.2 Mathematical formalism

The SM can be described within the formalism of quantum field theory (QFT) with the Lagrangian

$$\mathcal{L}_{\text{SM}} = \mathcal{L}_{\text{QCD}} + \underbrace{(\mathcal{L}_{\text{gauge}} + \mathcal{L}_{\text{fermion}} + \mathcal{L}_{\text{Higgs}} + \mathcal{L}_{\text{Yukawa}})}_{\mathcal{L}_{\text{EW}}} \qquad (2.1)$$

where $\mathcal{L}_{\text{QCD}}$ is the QCD term and $\mathcal{L}_{\text{EW}}$ is the electroweak (EW) term of the Lagrangian. Formalism of QFT within the SM treats particles as excitations [22] of their corresponding quantum fields i.e. fermion field ψ, electroweak boson fields $W_{1,2,3}$ & B, gluon fields G_α and Higgs field ϕ.

The foundation of modern QFT involves gauge theory. A quantum field has gauge symmetry if there exists a continuous gauge transformation that when applied to every point in a field (local gauge transformation) leaves the field Lagrangian unchanged. The set of gauge transformations of a gauge symmetry is the symmetry group of the field which comes with a set of generators, each with a correspoding gauge field. Under QFT, the quanta of these gauge fields are called gauge bosons.

The SM Lagrangian is gauge invariant under global Poincaré symmetry and local $SU(3)_C \times SU(2)_L \times U(1)_Y$ gauge symmetry, with the $SU(3)_C$ symmetry group corresponding to the strong interaction and $SU(2)_L \times U(1)_Y$ to the EW interaction. Global Poincaré symmetry ensures that $\mathcal{L}_{\text{SM}}$ satisfies translational symmetry, rotational symmetry and Lorentz boost frame invariance [23]. These symmetries give rise to corresponding conservation laws, which lead to conservation of momentum, angular momentum and energy in the SM as a result of Noether's theorem.

9

2.1.2.1 Quantum chromodynamics

468 Quantum chromodynamics is a non-Abelian gauge theory i.e. Yang-Mills theory [1, 2]

469 describing the strong interaction between quarks in the SM with the gauge group $SU(3)_C$,

470 where C represents conservation of color charge under $SU(3)_C$ symmetry. According to

471 QFT, quarks can be treated as excitations of the corresponding quark fields ψ. The free Dirac

472 Lagrangian for the quark fields $\mathcal{L}_0 = \bar{\psi}(i\gamma^\mu\partial_\mu - m)\psi$ is invariant under global $SU(3)$ sym-

473 metry, but not under local $SU(3)_C$ symmetry. To establish invariance under local $SU(3)_C$

474 symmetry, the gauge covariant derivative D_μ is defined so that

$$D_\mu\psi = (\partial_\mu - ig_s G_\mu^a T_a)\psi, \tag{2.2}$$

475 where $g_s = \sqrt{4\pi\alpha_s}$ is the QCD coupling constant, $G_\mu^a(x)$ are the eight gluon fields, and

476 T_a are generators of $SU(3)_C$, represented as $T_a = \lambda_a/2$ with λ_a being the eight Gell-Mann

477 matrices [15]. Let the gluon field strength tensors $G_{\mu\nu}^a$ be

$$G_{\mu\nu}^a \equiv \partial_\mu G_\nu^a - \partial_\nu G_\mu^a - g_s f^{abc} G_\mu^b G_\nu^c, \tag{2.3}$$

478 where f^{abc} are the structure constants of $SU(3)_C$. The gauge invariant QCD Lagrangian

479 can then be written as

$$\mathcal{L}_{\text{QCD}} = \bar{\psi}(i\gamma^\mu D_\mu - m)\psi - \frac{1}{4}G_{\mu\nu}^a G_a^{\mu\nu}$$

$$= \underbrace{-\frac{1}{4}G_{\mu\nu}^a G_a^{\mu\nu}}_{\substack{\text{gluon kinematics} \\ \text{\& self-interaction}}} + \underbrace{\bar{\psi}\left(i\gamma^\mu\partial\mu - m\right)\psi}_{\substack{\text{quark kinematics} \\ \text{\& masses}}} + \underbrace{\bar{\psi}^i\left(g_s\gamma^\mu(T_a)_{ij}G_\mu^a\right)\bar{\psi}^j}_{\text{quark-gluon interaction}}, \tag{2.4}$$

480 where i, j are color indices with integer values from 1 to 3. Gluons are forced to be massless

481 from the lack of a gluon mass term to maintain gauge invariance for the Lagrangian.

2.1.2.2 Electroweak theory

483 The electroweak interaction is the unified description of the weak interaction and electro-

484 magnetism under the $SU(2)_L \times U(1)_Y$ symmetry group, where L represents the left-handed

485 chirality of the weak interaction and Y represents the weak hypercharge quantum number.

486 Fermions can have either left-handed or right-handed chirality with the exception of neutri-

487 nos which can only have left-handed chirality in the SM, and can be divided into left-handed

488 doublets and right-handed singlets

$$\psi_L = \begin{pmatrix} \nu_e \\ e_L \end{pmatrix}, \begin{pmatrix} \nu_\mu \\ \mu_L \end{pmatrix}, \begin{pmatrix} \nu_\tau \\ \tau_L \end{pmatrix}, \begin{pmatrix} u_L \\ d_L \end{pmatrix}, \begin{pmatrix} c_L \\ s_L \end{pmatrix}, \begin{pmatrix} t_L \\ b_L \end{pmatrix}$$

$$\psi_R = e_R, \mu_R, \tau_R, u_R, d_R, c_R, s_R, t_R, b_R. \tag{2.5}$$

489 where g' is the B_μ coupling constant and $B_\mu(x)$ is a vector gauge field that transforms under

490 $U(1)_Y$ as

$$B_\mu \to B_\mu + \frac{1}{g'}\partial_\mu\theta(x). \tag{2.6}$$

491 Right-handed fermion singlets are not affected by $SU(2)_L$ transformation, so the fermion

492 fields ψ transform under $SU(2)_L$ as

$$\psi_L \to e^{iI_3\vec{\theta}(x)\cdot\vec{\sigma}/2}\psi_L$$

$$\psi_R \to \psi_R. \tag{2.7}$$

493 where $\vec{\sigma}/2$ are generators of $SU(2)_L$ with $\vec{\sigma}$ being the Pauli matrices. In order to preserve

494 local symmetry, the gauge covariant derivative for $SU(2)_L$ and $U(1)_Y$ can be defined [24] so

11

that the gauge covariant derivative for $SU(2)_L \times U(1)_Y$ can be written as

$$D_\mu \psi_L = \left(\partial_\mu - ig' \frac{Y_L}{2} B_\mu - ig \frac{\sigma_i}{2} W_\mu^i \right) \psi_L$$

$$D_\mu \psi_R = \left(\partial_\mu - ig' \frac{Y_R}{2} B_\mu \right) \psi_R. \tag{2.8}$$

where $B_\mu(x)$ is a vector gauge field associated with $U(1)_Y$ and $W_\mu^i(x)$ ($i = 1, 2, 3$) are three vector gauge fields associated with $SU(2)_L$. The B_μ and W_μ^i gauge fields transform under their corresponding symmetry groups $U(1)_Y$ and $SU(2)_L$ as

$$B_\mu \to B_\mu + \frac{1}{g'} \partial_\mu \theta(x)$$

$$W_\mu^i \to W_\mu^i + \frac{2}{g} \partial_\mu \theta_a(x) + \epsilon^{ijk} \theta_j(x) W_\mu^k, \tag{2.9}$$

where g' is the B_μ gauge coupling constant, g is the W_μ^i gauge coupling constants and ϵ^{ijk} is the $SU(2)_L$ structure constant. Similar to section 2.1.2.1, the kinetic term is added by defining field strengths for the four gauge fields

$$B_{\mu\nu} \equiv \partial_\mu B_\nu - \partial_\nu B_\mu$$

$$W_{\mu\nu}^i \equiv \partial_\mu W_\nu^i - \partial_\nu W_\mu^i - ge^{ijk} W_\mu^j W_\nu^k. \tag{2.10}$$

The local $SU(2)_L \times U(1)_Y$ invariant EW Lagrangian [24] is then

$$\mathcal{L}_{\text{EW}} = i\bar{\psi}(\gamma^\mu D_\mu)\psi - \frac{1}{4} W_{\mu\nu}^i W_i^{\mu\nu} - \frac{1}{4} B_{\mu\nu} B^{\mu\nu}$$

$$= \underbrace{i\bar{\psi} \left(\gamma^\mu \partial_\mu \right) \psi}_{\substack{\text{fermion} \\ \text{kinematics}}} \underbrace{- \bar{\psi} \left(\gamma^\mu g' \frac{Y}{2} B_\mu \right) \psi - \bar{\psi}_L \left(\gamma^\mu g \frac{\sigma_i}{2} W_\mu^i \right) \psi_L}_{\text{fermion-gauge boson interaction}} \underbrace{- \frac{1}{4} W_{\mu\nu}^i W_i^{\mu\nu} - \frac{1}{4} B_{\mu\nu} B^{\mu\nu}}_{\substack{\text{boson kinematics} \\ \text{\& self-interaction}}}.$$

$$\tag{2.11}$$

Under ≈ 159.5 GeV, the EW symmetry $SU(2)_L \times U(1)_Y$ undergoes spontaneous symmetry breaking [25] into $U(1)_{\text{QED}}$ symmetry, which corresponds to a separation of the weak and electrodynamic forces. Electroweak spontaneous symmetry breaking replaces the four massless and similarly-behaved EW gauge bosons B_μ and W^i_μ with the EM boson γ and the weak bosons $Z/W^\pm$, as well as giving the Z and $W^\pm$ bosons masses via the Higgs mechanism. This is due to a specific choice of gauge for the Higgs field leading to the reparameterization of the EW bosons B_μ and W^i_μ to $W^\pm/Z/\gamma$ using the relations

$$
W^\pm_\mu \equiv \frac{1}{\sqrt{2}} \left(W^1_\mu \mp i W^2_\mu \right)
$$

$$
\begin{pmatrix} A_\mu \\ Z_\mu \end{pmatrix} \equiv \begin{pmatrix} \cos\theta_{\text{W}} & \sin\theta_{\text{W}} \\ -\sin\theta_{\text{W}} & \cos\theta_{\text{W}} \end{pmatrix} \begin{pmatrix} B_\mu \\ W^3_\mu \end{pmatrix}
\tag{2.12}
$$

where $\theta_{\text{W}} \equiv \cos^{-1}\left(g/\sqrt{g^2 + g'^2} \right)$ is the weak mixing angle. The boson kinetic term can also be refactorized to extract cubic (three vertices) and quartic (four vertices) self-interactions among the gauge bosons [24]. The Lagrangian can then be rewritten as

$$
\mathcal{L} = \underbrace{e A_\mu \bar{\psi} \left(\gamma^\mu Q \right) \psi}_{\text{electromagnetism}} + \underbrace{\frac{e}{2\sin\theta_{\text{W}} \cos\theta_{\text{W}}} \bar{\psi} \gamma^\mu \left(v_f - a_f \gamma_5 \right) \psi Z_\mu}_{\text{neutral current interaction}}
$$

$$
+ \underbrace{\frac{g}{2\sqrt{2}} \sum_{\psi_L} \left[\bar{f}_2 \gamma^\mu \left(1 - \gamma_5 \right) f_1 W^+_\mu + \bar{f}_1 \gamma^\mu \left(1 - \gamma_5 \right) f_2 W^-_\mu \right]}_{\text{charged current interaction}}
\tag{2.13}
$$

$$
+ \mathcal{L}_{\text{kinetic}} + \underbrace{\mathcal{L}_{\text{cubic}} + \mathcal{L}_{\text{quartic}}}_{\text{boson self-interaction}}
$$

where $\gamma_5 = i\gamma^0 \gamma^1 \gamma^2 \gamma^3$ is the chirality projection operator, $a_f = I_3$, $v_f = I_3(1 - 4|Q|\sin^2\theta_{\text{W}})$ and f_1, f_2 are up and down type fermions of a left-handed doublet.

2.1.2.3 Higgs mechanism

So far, the EW bosons are massless since the mass terms $-m\bar{\psi}\psi$ for fermions and $-mA^\mu A_\mu$ for bosons are not invariant under the EW Lagrangian symmetries. The particles must then acquire mass under another mechanism. The Brout-Engler-Higgs mechanism [3–5] was introduced in 1964 to rectify this issue and verified in 2012 with the discovery of the Higgs boson [6, 7].

The Higgs potential is expressed as

$$V(\phi^\dagger \phi) = \mu^2 \phi^\dagger \phi + \lambda (\phi^\dagger \phi)^2 \tag{2.14}$$

where μ^2 and $\lambda > 0$ are arbitrary parameters, and the $SU(2)_L$ doublet $\phi = \begin{pmatrix} \phi^+ \\ \phi^0 \end{pmatrix}$ is the Higgs field with complex scalar fields ϕ^+ and ϕ^0 carrying $+1$ and 0 electric charge respectively. The Lagrangian for the scalar Higgs field is

$$\mathcal{L}_H = \left(\partial_\mu \phi\right)^\dagger \left(\partial^\mu \phi\right) - V\left(\phi^\dagger \phi\right). \tag{2.15}$$

Since the potential $V(\phi^\dagger \phi)$ is constrained by $\lambda > 0$, the ground state is solely controlled by μ. If $\mu^2 > 0$, the ground state energy is $\phi = 0$, and the EW bosons would remain massless. If $\mu^2 < 0$, the ground state is

$$|\phi|^2 = -\frac{\mu^2}{2\lambda} \equiv \frac{v^2}{\sqrt{2}}, \tag{2.16}$$

where v is defined as the vacuum expectation value (VEV). The standard ground state for the Higgs potential without loss of generality can be chosen as $\phi(0) = 1/\sqrt{2}\begin{pmatrix} 0 \\ v \end{pmatrix}$.

Having $U(1)$ symmetry allows any $-e^{i\theta}\sqrt{\mu^2/\lambda}$ to be a ground state energy for the Higgs

14
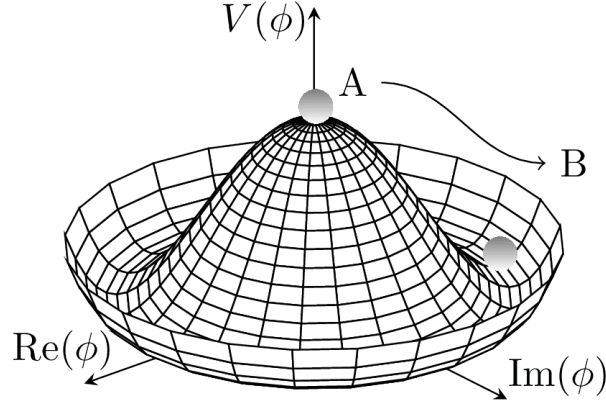
Figure 2.3: Illustration of a common representation of the Higgs potential [26]. Before SSB, the ground state $\phi(0)$ is located at A which is symmetric with respect to the potential. A perturbation to this state fixes the ground state energy $|\phi(0)|^2$ to a particular value at B, "spontaneously" breaking the symmetry and degeneracy in $|\phi(0)|^2$.

Lagrangian. This degeneracy results in spontaneous symmetry breaking of the $SU(2)_L \times U(1)_Y$ symmetry into $U(1)_{\text{EM}}$ symmetry when the Higgs field settles on a specific vacuum state as a result of a perturbation or excitation (Figure 2.3). The spontaneous symmetry breaking introduces three massless (Nambu-Goldstone [27]) vector gauge boson ξ and a massive scalar boson η, each corresponds to a generator of the gauge group. The vector field for ξ and η are real fields parameterized as $\xi \equiv \phi^+\sqrt{2}$ and $\eta \equiv \phi^0\sqrt{2} - v$ [28]. The Higgs field now becomes

$$\phi = \frac{v + \eta + i\xi}{\sqrt{2}} = \frac{1}{\sqrt{2}}e^{i\xi \cdot \frac{\sigma}{2v}}\begin{pmatrix} 0 \\ v + \eta \end{pmatrix}. \tag{2.17}$$

Due to $U(1)_{\text{EM}}$ invariance, a unitary gauge with the transformation $\phi \rightarrow \exp(-i\xi\cdot)\frac{\sigma}{2v}$ can be chosen for the Higgs field to eliminate the massless bosons and incorporate them into the EM/weak bosons via Equation 2.12. This leaves the massive η which can now be observed as an excitation of the Higgs field from the standard ground state and must be the Higgs boson h. Using the EW covariant derivative from Equation 2.8, the Higgs Lagrangian around the

15

vacuum state becomes

$$\mathcal{L}_H = \left(D_\mu \phi\right)^\dagger \left(D^\mu \phi\right) - \mu^2 \left(\frac{v+h}{\sqrt{2}}\right)^2 - \lambda \left(\frac{v+h}{\sqrt{2}}\right)^4$$
$$= \left(D_\mu \phi\right)^\dagger \left(D^\mu \phi\right) - \frac{1}{2}\mu^2 h^2 - \lambda v h^3 - \frac{\lambda}{4}h^4 - \dots . \tag{2.18}$$

The Higgs mass can be extracted from the quadratic term as $m_H = \sqrt{-2\mu^2}$. The kinetic term in the Lagrangian can be written as

$$\left(D_\mu \phi\right)^\dagger \left(D^\mu \phi\right) = \frac{1}{2}(\partial_\mu h)^2 + \frac{g^2}{8}(v+h)^2 \left| W_\mu^1 - i W_\mu^2 \right|^2 + \frac{1}{8}(v+h)^2 \left(g' W_\mu - g B_\mu\right)$$
$$= \frac{1}{2}(\partial_\mu h)^2 + (v+h)^2 \left(\frac{g^2}{4}W_\mu^+ W^{-\mu} + \frac{1}{8}\left(g^2 + g'^2\right) Z_\mu^0 Z^{0\mu}\right) . \tag{2.19}$$

Masses for the EW bosons can be extracted from the quadratic terms

$$m_{W^\pm} = \frac{v}{2}g , \qquad m_Z = \frac{v}{2}\sqrt{g^2 + g'^2} , \qquad m_\gamma = 0. \tag{2.20}$$

However, the fermion mass term $-m\bar{\psi}\psi$ still breaks EW invariance after spontaneous symmetry breaking. Instead, fermions acquire mass by replacing the mass term with a gauge invariant Yukawa term in the EW Lagrangian representing fermions' interactions with the Higgs field [28]

$$\mathcal{L}_{\text{Yukawa}} = -c_f \frac{v+h}{\sqrt{2}}\left(\bar{\psi}_R \psi_L + \bar{\psi}_L \psi_R\right)$$
$$= -\underbrace{\frac{c_f}{\sqrt{2}}v(\bar{\psi}\psi)}_{\text{fermion mass}} - \underbrace{\frac{c_f}{\sqrt{2}}(h\bar{\psi}\psi)}_{\text{fermion-Higgs interaction}} , \tag{2.21}$$

where c_f is the fermion-Higgs Yukawa coupling. The fermion mass is then $m_f = c_f v/\sqrt{2}$.

16

2.2 Beyond the Standard Model

2.2.1 Top-philic vector resonance

Many BSM models extend the SM by adding to the SM gauge group additional $U(1)'$ gauge symmetries [29], each with an associated vector gauge boson nominally called Z'. In the case of a BSM global symmetry group with rank larger than the SM gauge group, the symmetry group can spontaneously break into $G_{\text{SM}} \times U(1)'^n$, where G_{SM} is the SM gauge group $SU(3)_C \times SU(2)_L \times U(1)_Y$ and $U(1)'^n$ is any $n \geq 1$ number of $U(1)'$ symmetries. The existence of additional vector bosons Z' would open up many avenues of new physics e.g. extended Higgs sectors from $U(1)'$ symmetry breaking [30, 31], existence of flavor-changing neutral current (FCNC) mediated by Z' [32], and possible exotic production from heavy Z' decays [33].

Due to the top quark having the largest mass out of all known elementary particles in the SM, many BSM models [34–37] predict 'top-philic' vector resonances that have much stronger coupling to the top quark compared to other quarks. The analysis in this dissertation attempts to reconstruct a top-philic Z' resonance directly to avoid dependency on model choice. Previous model-independent BSM $t\bar{t}t\bar{t}$ search for top-philic resonances [9] in the single-lepton final state and similar mass ranges showed upper limits on observed (expected) Z' production cross section between 21 (14) fb to 119 (86) fb depending on parameter choice. This analysis is also motivated by the recent observation of SM $t\bar{t}t\bar{t}$ production in the same-sign multilepton (SSML) channel by ATLAS [10] and CMS [38] at 6.1σ and 5.6σ discovery significance respectively.

In addition to the model-independent search, a simplified color-singlet vector particle

model [11, 39] is employed to study model-dependent interpretations. The interaction Lagrangian assumes only Z' to top coupling and has the form

$$
\begin{aligned}
\mathcal{L}_{Z'} &= \bar{t}\gamma_\mu \left(c_L P_L + c_R P_R\right) t Z'^\mu \\
&= c_t \bar{t}\gamma_\mu \left(\cos\theta P_L + \sin\theta P_R\right) t Z'^\mu,
\end{aligned}
\tag{2.22}
$$

where $c_t = \sqrt{c_L^2 + c_R^2}$ is the Z'-top coupling strength, $P_{L/R} = (1 \mp \gamma_5)/2$ are the chirality projection operators, and $\theta = \tan^{-1}(c_R/c_L)$ is the chirality mixing angle. Expanding the Lagrangian results in

$$
\mathcal{L}_{Z'} = \frac{1}{\sqrt{2}}\bar{t}\gamma_\mu \left[\sin\left(\theta + \frac{\pi}{4}\right) - \left(\sqrt{2}\cos\left(\theta + \frac{\pi}{4}\right)\right)\gamma_5\right] t Z'^\mu,
\tag{2.23}
$$

which bears striking resemblance to the EW Lagrangian neutral current interaction term in Equation 2.13, showing the similarity between the Z' and the Z boson that acquires mass from $SU(2)_L \times U(1)_Y$ spontaneous symmetry breaking. Assuming the Z' mass $m_{Z'}$ is much larger than the top mass ($m_t^2/m_{Z'}^2 \approx 0$), the Z' decay width at leading-order (LO) can be approximated as

$$
\Gamma(Z' \to t\bar{t}) \approx \frac{c_t^2 m_{Z'}}{8\pi}.
\tag{2.24}
$$

It can be observed that $\Gamma/m_{Z'} \approx c_t^2/8\pi \ll 1$ for $c_t \approx 1$, which suggests a very narrow and well-defined resonance peak. This validates the narrow-width approximation for the choice of $c_t = 1$ and supports efforts to directly reconstruct the resonance.

The main production channels for the aforementioned heavy top-philic color singlet Z' are at tree level and loop level, with the one-loop level being the dominant processes. Loop level processes are dependent on the chirality angle θ, where $\theta = \pi/4$ suppresses all but

18

gluon-initiated box sub-processes [11]. To minimize model dependence, only the tree level production was considered for this analysis by choosing $\theta = \pi/4$. Figure 2.4 illustrates several tree level Z' production processes.

(a) $t\bar{t}Z'$ (b) tjZ' (c) tWZ'
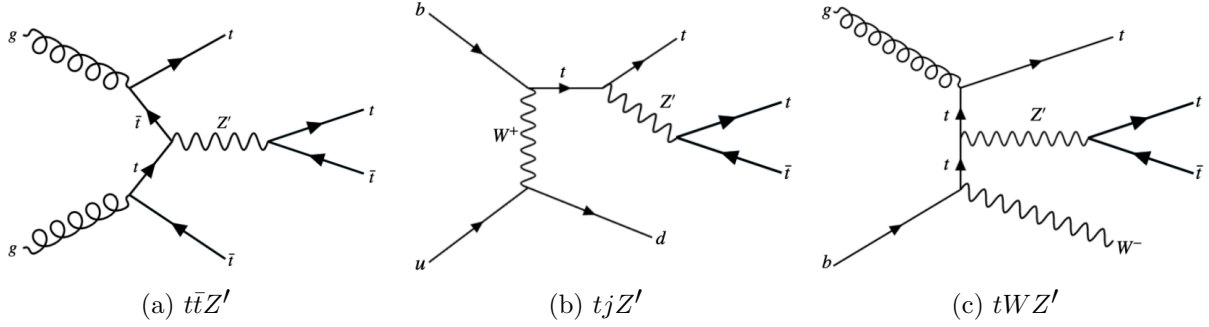
Figure 2.4: Feynman diagrams for tree level Z' production in association with (a) $t\bar{t}$, (b) tj (light quark) and (c) tW, decaying to final states containing (a) $t\bar{t}t\bar{t}$ or (b)(c) $t\bar{t}t$ [11].

The single-top-associated channels tjZ' and tWZ' are suppressed by three-body phase space [11], resulting in smaller cross sections by a factor of two compared to the $t\bar{t}$-associated process $t\bar{t}Z'$. Unlike tjZ' and tWZ' which are produced via EW and mixed QCD-EW interactions respectively, $t\bar{t}t\bar{t}$ production is governed by the strong interaction which can overpower phase space suppression. Additionally, $t\bar{t}t\bar{t}$ production is independent of θ while tjZ' and tWZ' are minimally suppressed under pure left-handed interactions ($\theta = 0$) and maximally suppressed under pure right-handed interactions ($\theta = \pi/2$).

2.2.2 BSM four-top quark production

This analysis uses the $t\bar{t}t\bar{t}$ final state signal signature to search for the existence of a heavy BSM resonance that couples strongly to the top quark. Cross section for $t\bar{t}t\bar{t}$ production can be enhanced by many possible BSM models, in particular two-Higgs-doublet models (2HDM) [40–42] or possible production of a heavy neutral resonance boson $Z'(\to t\bar{t})$ in association with a $t\bar{t}$ pair in composite Higgs scenarios [34, 35]. The $t\bar{t}Z'$ production mode

⁶⁰⁶ and consequently $t\bar{t}t\bar{t}$ signal signature can provide a more sensitive channel for searches by

⁶⁰⁷ avoiding contamination from the large SM $gg \to t\bar{t}$ background in an inclusive $Z' \to t\bar{t}$

⁶⁰⁸ search.

Decay modes

⁶¹⁰ The different W boson decay modes

⁶¹¹ shown in Figure 2.2 result in many differ-

⁶¹² ent final states for $t\bar{t}Z'/t\bar{t}t\bar{t}$ decay, which

⁶¹³ can each be classified into one of three chan-

⁶¹⁴ nels shown in Figure 2.5: all hadronic de-

⁶¹⁵ cays; exactly one lepton or two opposite-sign

⁶¹⁶ leptons (1LOS); exactly two same-sign lep-

⁶¹⁷ tons or three or more leptons (SSML). The

⁶¹⁸ branching ratio for each channel is shown

⁶¹⁹ in Figure 2.5. The all hadronic and 1LOS

⁶²⁰ channels have much larger branching ratios

Figure 2.5: Branching ratios for $t\bar{t}t\bar{t}$ decay [43]. The same-sign dilepton and multilepton channels together forms the SSML channel.

⁶²¹ compared to SSML channel but suffer heavily from $gg \to t\bar{t}$ background contamination,

⁶²² giving the SSML channel better sensitivity at the cost of lower statistics. This is also the

⁶²³ targeted channel for this analysis.

Chapter 3. LHC & ATLAS Experiment

3.1 The Large Hadron Collider

Predictions from theoretical models are evaluated against experimental data collected from particle detectors. This chapter provides a detailed overview of the Large Hadron Collider (LHC) and the ATLAS detector, one of the key experiments designed to study high-energy collisions at the LHC.

3.1.1 Overview

The Large Hadron Collider [44] (LHC) is currently the world's largest particle collider with a circumference of almost 27 km. Built by CERN on the border of Switzerland and France, the LHC is designed as a particle collider for proton-proton (pp), sometimes heavy ions i.e. lead-lead (PbPb) and proton-lead (pPb) beams at TeV-scale energies. Two beams of particles are injected into the LHC in opposite directions and allowed to collide at the center of four major experiments:

- **A Toroidal LHC ApparatuS** (ATLAS) [45] and **Compact Muon Solenoid** (CMS) [46]: multi-purpose detectors, designed to target a variety of phenomena including SM, BSM and heavy-ion physics.

- **Large Ion Collider Experiment** (ALICE) [47]: specialized detector to record ion collisions and study heavy-ion physics.

- **Large Hadron Collider beauty** (LHCb) [48]: detector dedicated to study properties of b-quarks and b-hadrons.

21

⁶⁴⁴ Aside from the four major experiments, the LHC also houses smaller experiments e.g.

⁶⁴⁵ AWAKE [49], FASER [50], KATRIN [51], that either share an interaction point with one of

⁶⁴⁶ the above experiments or make use of particle beams pre-LHC injection.
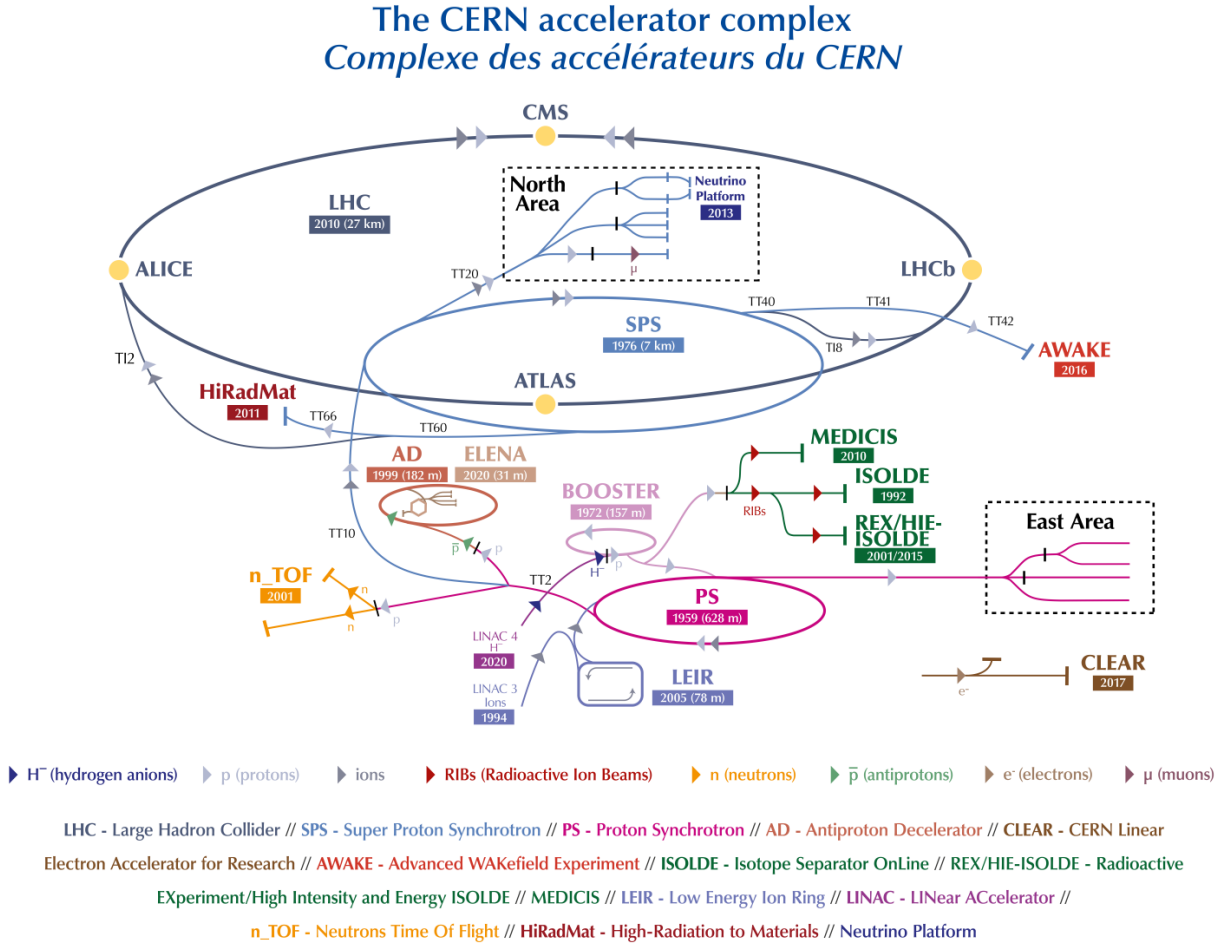
Figure 3.1: The full CERN accelerator complex as of 2022 [52].

⁶⁴⁷ The majority of the LHC operational time is dedicated to studying pp collisions of up to

⁶⁴⁸ $\sim$13 TeV center-of-mass energy, denoted as $\sqrt{s}$. Reaching collision energy requires a sequence

⁶⁴⁹ of accelerators within the CERN accelerator complex, shown in Figure 3.1. Proton produc-

⁶⁵⁰ tion starts at LINAC 4, where hydrogen atoms are accelerated to 160 MeV then stripped

⁶⁵¹ of electrons. The leftover proton beams are injected into the Proton Synchrotron Booster

22

(PSB) and accelerated to 2 GeV before being transferred into the Proton Synchrotron (PS).

Here, the beams are ramped up to 26 GeV then injected into the Super Proton Synchrotron

(SPS) to further raise the energy threshold to 450 GeV. The beams are finally injected into

the LHC in opposite directions, continuously increasing in energy up to 6.5 TeV per beam,

reaching the 13 TeV center-of-mass energy threshold necessary for collision during Run 2.

As of the start of Run 3 in 2022, proton beams can now be ramped up to 6.8 TeV per beam

for a total of $\sqrt{s} = 13.6$ TeV.

3.1.2 LHC operations
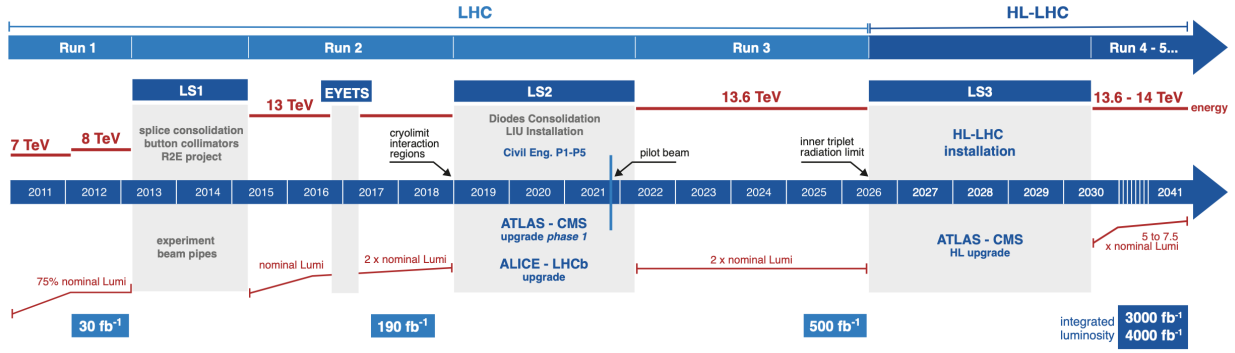
Figure 3.2: Current and future timeline of LHC operations with corresponding center-of-mass energies and projected integrated luminosities. [53].

Operations at the LHC are defined in periods of data-taking and shut-down known as

runs and long shutdowns respectively; the first period (Run 1) started with first collisions

at the LHC in 2010 at $\sqrt{s} = 7$ TeV [54]. Upgrades are usually carried out for detectors and

accelerators during long shutdowns, raising the maximum energy threshold in preparation

for the next run. An overview of the LHC runtime and corresponding center-of-mass energies

are summarized in Figure 3.2. During Run 2 from 2015-2018, the ATLAS detector recorded

a total of 1.1×10^{16} pp collisions at $\sqrt{s} = 13$ TeV, which corresponds to an integrated

luminosity of $140 \pm 0.83\%$ fb^{-1} that passed data quality control and are usable for analyses [55]. This is also the data set used for the analysis in this dissertation.

status/plan for run 3 and beyond?

3.1.3 Physics at the LHC

The majority of physics studied at the LHC focus primarily on QCD proton-proton hard scattering processes and the resulting products. Hard scattering processes involve large momentum transfer compared to the proton mass e.g. top pair production ($gg \rightarrow t\bar{t}$) and Higgs production ($gg \rightarrow H$), and can be predicted using perturbative QCD [56]. Hard processes probe distance scales much lower than the proton radius and can be considered collisions between the constituent quarks and gluons i.e. partons. Soft processes involve lower momentum transfer between partons and are dominated by less well-understood non-perturbative QCD effects. The hard interaction between two partons are represented by a parton distribution function (PDF) $f_i(x, Q^2)$, which describes the probability of interacting with a constituent parton i that carries a fraction x of the external hadron's momentum when probed at a momentum scale of Q^2 [57]. Other partons within the hadron that did not participate in the collision can still interact via lower momentum underlying-events (UE). The probability of a particular interaction occurring is defined as its cross-section $\sigma[b]$. Figure 3.3 gives an overview of SM processes produced within the LHC and their cross-sections.
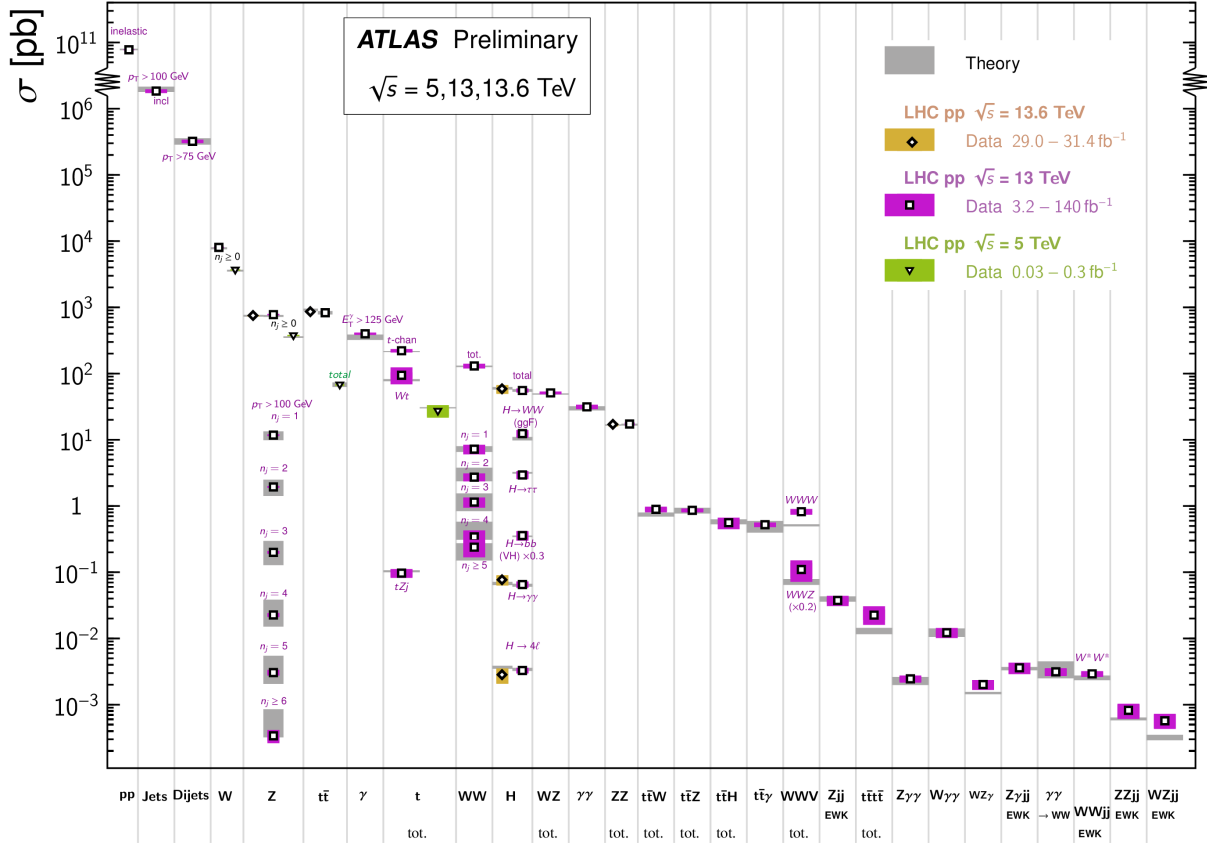
Figure 3.3: Summary of predicted and measured cross-section for SM processes at the LHC at different center-of-mass energies [58].

3.2 The ATLAS detector

One of the four main experiments at the LHC is ATLAS [45], designed as a multi-purpose detector for the role of studying high-energy physics in pp and heavy-ion collisions. ATLAS is a detector with symmetric cylindrical geometry with dimensions of 44 m in length and 25 m in diameter, covering a solid angle of almost 4π around the collision point. The detector is built concentrically around the beamline with the collision point at the center to maximally capture signals produced by interactions. Figure 3.4 shows a slice of the ATLAS detector.

From the inside out, the main ATLAS subdetector system consists of the inner detector
(ID), calorimeter systems (electromagnetic and hadronic) and the muon spectrometer (MS).
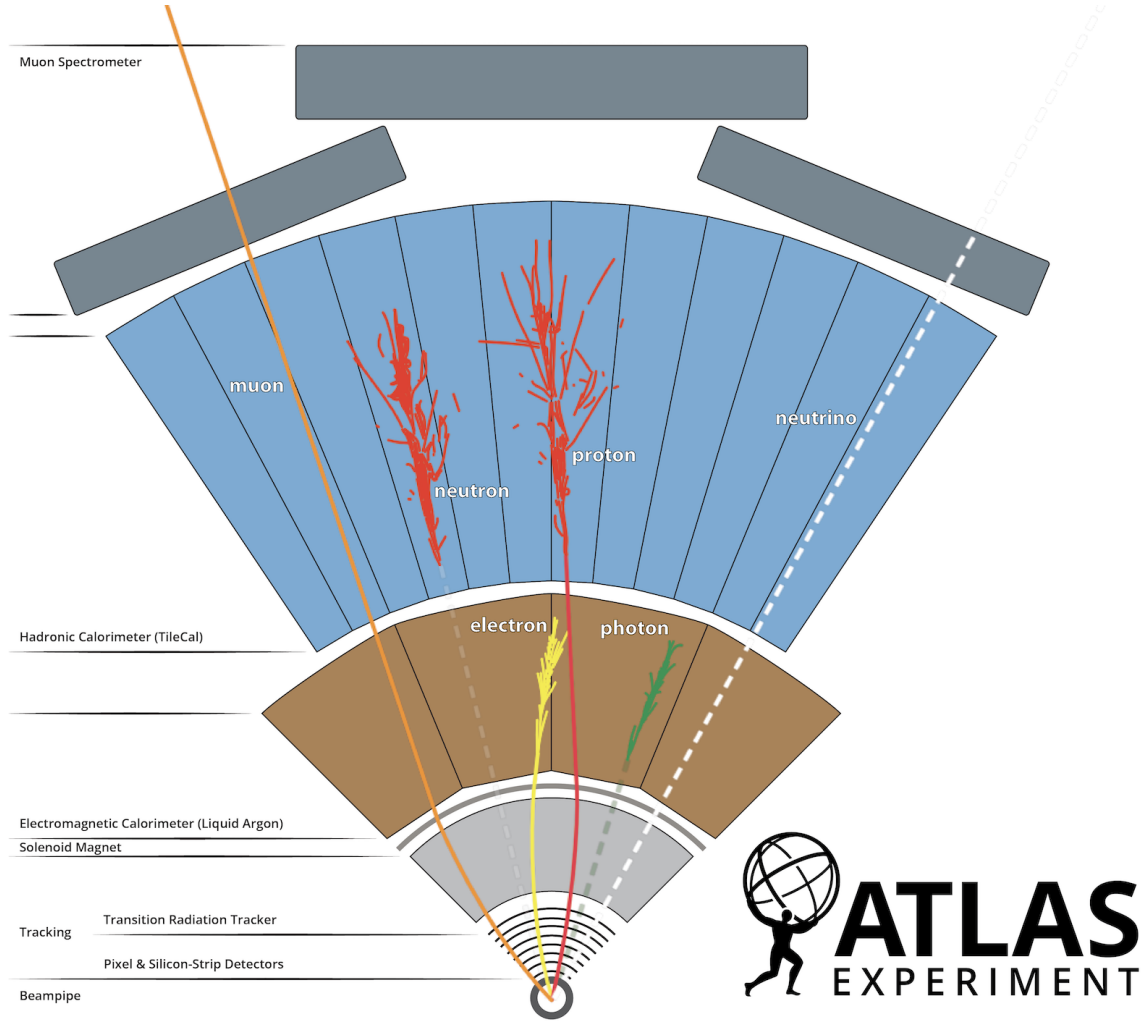
Figure 3.4: A cross section slice of the ATLAS detector showing different subsystems along
with visualization of different types of particles traveling through the detector [59].

The ATLAS detector uses a right-handed coordinate system [45] designed to align with
the geometry of a collision interaction, with the origin set at the interaction point, the z-axis
following (either of) the beamline and the x-axis pointing towards the center of the LHC
ring. In cylindrical coordinates, the polar angle θ is measured from the beam axis, and
the azimuthal angle ϕ is measured along the transverse plane (xy-plane) starting at the x-

axis. Addtional observables are defined for physics purposes: the pseudorapidity defined as $\eta = -\ln\tan(\theta/2)$; angular distance within the detector defined as $\Delta R = \sqrt{\Delta\eta^2 + \Delta\phi^2}$; and transverse momentum p_{T} (transverse energy E_{T}) defined as the component of the particle's momentum (energy) projected onto the transverse plane.

3.2.1   Inner detector

The innermost part of ATLAS is the inner detector (ID) [45], constructed primarily for the purpose of measuring and reconstructing charged tracks within the $|\eta| < 2.5$ region with high momentum resolution ($\sigma_{p_{\mathrm{T}}}/p_{\mathrm{T}} = 0.05\% \pm 1\%$). Figure 3.5 shows the composition of the ID with three subsystems, the innermost being the pixel detector, then Semiconductor Tracker (SCT), and the Transition Radiation Tracker (TRT) on the outermost layer; all of which are surrounded by a solenoid magnet providing a magnetic field of 2 T.
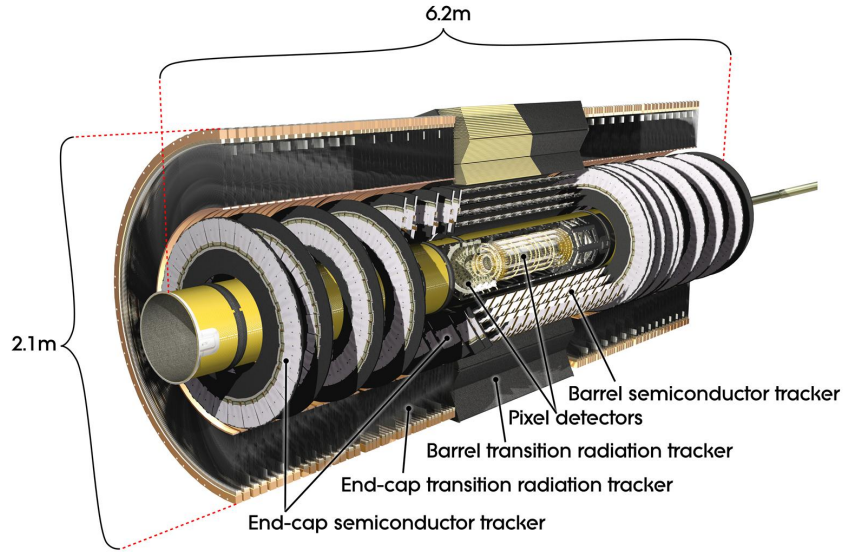
Figure 3.5: Cutaway illustration of the inner detector along with its subsystems [60].

27

Pixel detector

The pixel detector subsystem [45] consists of 250 µm silicon semiconductor pixel layers with about 80.4 million readout channels, reaching a spatial resolution of 10 µm in the $R-\phi$ (transverse) plane and 115 µm in the z-direction for charged tracks. Charged particles passing through the pixel detector ionize the silicon layers and produce electron-hole pairs; the electrons drift towards the detector's electrode under an applied electric field and the resulting electric signals are collected in read-out regions. The pixel detector is used primarily for impact parameter measurement, pile-up suppression, vertex finding and seeding for track reconstruction.

Semiconductor Tracker

The Semiconductor Tracker (SCT) [45] functions similarly to the pixel detector, using silicon semiconductor microstrips totaling about 6.3 million read-out channels, reaching a per layer resolution of 17 µm in the R-ϕ plane and 580 µm in the z-direction [45]. The SCT plays an important role in precise p_T measurement of charged particles as well as track reconstruction.

Transition Radiation Tracker

The outermost layer of the ID, the Transition Radiation Tracker (TRT) [45], consists of layers of 4 mm diameter straw tubes filled with a xenon-based gas mixture and a 30 µm gold-plated wire in the center. The TRT contains a total of about 351 thousand readout channels with a resolution of 130 µm for each straw tube in the R-ϕ plane, and provides extended track measurement, particularly estimation of track curvature under the solenoidal

magnetic field. Importantly, the TRT also serves to identify electrons through absorption of emitted transition-radiation within the Xe-based gas mixture.

3.2.2   Calorimeter systems

Surrounding the ID is the ATLAS calorimeter system [45] with electromagnetic (EM) and hadronic calorimeters, covering a range of $|\eta| < 4.9$. The calorimeters are sampling calorimeters with alternating absorbing layers to stop incoming particles and active layers to collect read-out signals from energy deposits. Incoming particles passing through the calorimeters interact with the absorbing layers, producing EM or hadronic showers of secondary particles. The particle showers deposit energy in the corresponding layer of the calorimeters, which are collected and aggregated to identify and reconstruct the original particle's energy and direction. Figure 3.6 shows a schematic overview of the ATLAS calorimeter system.
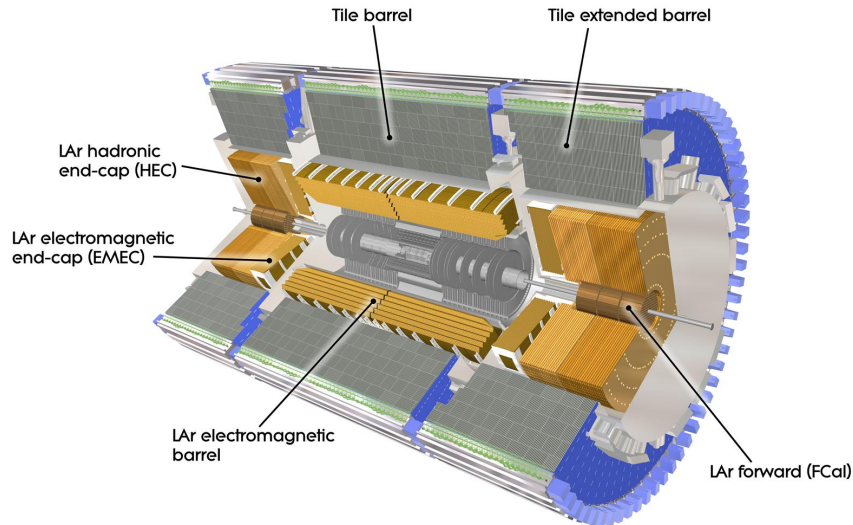
Figure 3.6: Cutaway illustration of the calorimeter system including the EM, hadronic and LAr forward calorimeters [61].

Electromagnetic calorimeter

The EM calorimeter [45] covers the innermost part of the calorimeter system, with lead (Pb) absorbing layers and liquid argon (LAr) active layers to capture the majority of electrons and photons exiting the ID. The EM calorimeter is divided into regions depending on η coverage: a barrel region ($|\eta| < 1.475$), two endcap regions ($1.375 < |\eta| < 3.2$) and a transition region ($1.372 < |\eta| < 1.52$). The endcap calorimeters are further divided into an outer wheel region ($1.372 < |\eta| < 2.5$) and an inner wheel region ($2.5 < |\eta| < 3.2$) in order to provide precise coverage within the same η range as the ID. Overlap between the barrel and endcap regions compensates for the lower material density in the transition region.

Hadronic calorimeter

The hadronic calorimeter [45] covers up to $|\eta| < 4.9$ and is comprised of three parts: the tile calorimeter with a barrel region ($|\eta| < 1.0$) and extended barrel regions ($0.8 < |\eta| < 1.7$); the hadronic endcap calorimeter (HEC) covering $1.5 < |\eta| < 3.2$; and the forward calorimeter (FCal) covering $3.2 < |\eta| < 4.9$. The tile calorimeter covers the EM calorimeter barrel region and uses steel as material for the absorbing layers with scintillating tiles for the active layers. Signals captured by scintillating tiles are read out from both sides using photomultiplier tubes. The HEC calorimeter covers the endcap regions of the EM calorimeter and uses a copper-LAr calorimeter layer scheme. The FCal is located close to the beamline providing coverage for particles traveling close to parallel with the beam axis. The subdetector contains three modules: one with copper absorbing layers optimized for EM measurements, and two with tungsten absorbing layers targeting hadronic cascades. All modules in the FCal use LAr as the active layer.

3.2.3 Muon spectrometer

Generally, the only particles that penetrate past the calorimeter layer are muons and neutrinos. The muon spectrometer (MS) [45] is situated on the outermost of the ATLAS detector and aims to track and measure muons within $|\eta| < 2.7$. The MS utilizes an array of toroid magnets to provide a magnetic field perpendicular to the muon trajectory, bending the track in order to measure its curvature. The magnetic field is powered by a large barrel toroid ($|\eta| < 1.4$) with strength of 0.5 T and two endcap toroid magnets ($1.6 < |\eta| < 2.7$) of 1 T. Both types contribute to the magnetic field in the transition region ($1.4 < |\eta| < 1.6$).

To measure the muon itself, four types of large gas-filled chambers known as muon chambers [45] are designed and constructed for two main goals: triggering on potential muon candidates entering the MS and tracking their trajectories through the detector with high precision. The tracking system include Monitored Drift Tubes (MDTs), which record muon track information over the entire MS η range ($|\eta| < 2.7$). The MDTs are built with multiple layers of drift tubes and filled with a mixture of 93% Ar and 7% CO_2. Muons passing through drift tubes in the MDT ionize the gas within each tube; signals are then recorded as freed electrons drift to read-out channels under an applied electric field. In the forward region ($2.0 < |\eta| < 2.7$), Cathode Strip Chambers (CSCs) are included along with MDTs. The CSCs are multiwire proportional chambers built with higher granularity and shorter drift time than the MDTs to handle tracking in an environment with high background rates .

The MS trigger system includes Resistive Plate Chambers (RPCs) [45], which provide triggering in the barrel region ($|\eta| < 1.05$) using parallel electrode plates made of resistive materials with a gas mixture inbetween. High voltage is applied to the plates, accelerat-

ing the electrons freed from ionized gas and creating a fast avalanche of charge, which is collected on external read-out strips almost instantaneously. Triggering and coarse position measurements in the endcap region ($1.05 < |\eta| < 2.5$) is handled by Thin-Gap Chambers (TGCs). Similar to CSCs, TGCs are multiwire proportional chambers with a small wire gap ("thin-gap") and high applied voltage across the gap, resulting in fast response time giving TGCs the capabilities to identify muon candidates in real time.

3.2.4 Trigger & data acquisition

The LHC produces a colossal amount of collision data at a bunch crossing rate of 40 MHz with bunch spacing of 25 ns. The ATLAS Trigger and Data Acquisition (TDAQ) system [62] synchronously identifies and records interesting events for in-depth analysis. The ATLAS trigger system in Run 2 consists of two steps: Level-1 (L1) trigger and High-Level Trigger (HLT). Events failing any step in the trigger chain are permanently lost.

The L1 trigger hardware is divided into L1 calorimeter triggers (L1Calo) and L1 muon triggers (L1Muon) [62]. L1Calo trigger uses information from ATLAS calorimeter system to quickly identify signs of high p_T objects e.g. EM clusters, jets and missing transverse energy $E_\mathrm{T}^\mathrm{miss}$ (section 4.4). Similarly, L1Muon uses information from the RPCs and TGCs of the MS to make quick decisions on potentially interesting muon candidates. Outputs from L1Calo and L1Muon are fed into the L1 topological trigger (L1Topo) for additional filtering based on event topology and multi-object correlation, allowing for more selective and physics-motivated triggering. Decisions from all three types of L1 triggers are provided as inputs for the Central Trigger Processor (CTP) for a final Level-1 Accept (L1A) decision. The entire L1 trigger chain results in a 2.5 μs latency and reduces the event rate to 100 kHz.

Events passing L1 triggers are sent to HLTs before being saved to offline storage at

CERN data centers. HLTs are software-based triggers used for more complex and specific selections on physics objects required by targeted analysis goals, in turn requiring more computing power with longer latency. After HLT selections, the event rate is reduced to 1 kHz on average [62]. Overall, the full trigger chain reduces the event rate for ATLAS by approximately a factor of 4×10^4.

Chapter 4. Particle Reconstruction & Identification

Activity within the ATLAS detector is recorded as raw electronic signals, which can be utilized by ATLAS reconstruction software to derive physics objects for analysis. This chapter describes the reconstruction and identification of basic objects (e.g. interaction vertices, tracks, topological clusters of energy deposits) and subsequently of complex physics objects i.e. particles and particle signatures.

4.1 Primary reconstruction

4.1.1 Tracks

Charged particles traveling through the ATLAS detector deposit energy in different layers of the ID and MS. The ID track reconstruction software consists of two algorithm chains: inside-out and outside-in track reconstruction [63–65].

The inside-out algorithm is primarily used for the reconstruction of primary particles i.e. particles directly produced from pp collisions or decay products of short-lived particles. The process starts by forming space points from seeded hits in the silicon detectors within the pixel & SCT detectors. Hits further away from the interaction vertex are added to the track candidate using a combinatorial Kalman filter [66] pattern recognition algorithm. Track candidates are then fitted with a χ^2 filter [67] and loosely matched to a fixed-sized EM cluster. Successfully matched track candidates are re-fitted with a Gaussian-sum filter (GSF) [68], followed by a track scoring strategy to resolve fake tracks & hit ambiguity

between different tracks [69]. The track candidate is then extended to the TRT to form final tracks satisfying $p_\mathrm{T} > 400$ MeV. The outside-in algorithm handles secondary tracks mainly produced from long-lives particles or decays of primary particles by back-tracking from TRT segments, which are then extended inward to match silicon hits in the pixel and SCT detectors to form track reconstruction objects.

4.1.2 Vertices

Vertices represent the point of interaction or decay for particles within the ATLAS detector. Primary vertices (PVs) are defined as the point of collision for hard-scattering pp interactions, while secondary or displaced vertices result from particle decays occurring at a distance from its production point.

Reconstruction of PVs is crucial to accurately profile the kinematic information of an event and form a basis for subsequent reconstruction procedures. Primary vertex reconstruction occurs in two stages: vertex finding and vertex fitting [70]. The vertex finding algorithm uses the spatial coordinates of reconstructed tracks to form the seed for a vertex candidate. An adaptive vertex fitting algorithm [71] then iteratively evaluates track-vertex compatibility to estimate a new best vertex position. Less compatible tracks are down-weighted in each subsequent iteration, and incompatible tracks are removed and can be used for another vertex seed; the process is repeated until no further PV can be found. All reconstructed vertices without at least two matched tracks are considered invalid and discarded.

Secondary vertex reconstruction uses the Secondary Vertex Finder (SVF) algorithm [72] which is primarily designed to reconstruct b- and c-hadrons for flavor tagging purposes. The SVF aims to reconstruct one secondary vertex per jet and only considers tracks that

35

are matched to a two-track vertex and contained within a p_T-dependent cone around the jet axis. The tracks are then used to reconstruct a secondary vertex candidate using an iterative process similar to the PV vertex fitting procedure.

Pile-up

At high luminosities, multiple interactions can be associated with one bunch crossing, resulting in many PVs. The effect is called pile-up [73], and usually result from soft QCD interactions. Pile-up can be categorized into two types: in-time pile-up, stemming from additional pp collisions in the same bunch crossing that is not the hard-scatter process; out-of-time pile-up, resulting from leftover energy deposits in the calorimeters from other bunch crossings.

4.1.3 Topological clusters

Topological clusters (topo-clusters) [74] consist of clusters of spatially related calorimeter cell signals. Topo-clusters are primarily used to reconstruct hadron- and jet-related objects in an effort to extract signal while minimizing electronic effects and physical fluctuations, and also allow for recovery of energy lost through bremsstrahlung or photon conversions. Cells with signal-to-noise ratio $\varsigma_{\text{cell}}^{\text{EM}}$ passing a primary seed threshold are seeded into a dynamic topological cell clustering algorithm as part of a proto-cluster. Neighboring cells satisfying a cluster growth threshold are collected into the proto-cluster. If a cell is matched to two proto-clusters, the clusters are merged. Two or more local signal maxima in a cluster satisfying $E_{\text{cell}}^{\text{EM}} > 500$ MeV suggest the presence of multiple particles in close proximity, and the cluster is split accordingly to maintain good resolution of the energy flow. The process continues iteratively until all cells with $\varsigma_{\text{cell}}^{\text{EM}}$ above a principal cell filter level have been matched to a

cluster.

(a) Cells passing primary seed threshold

(b) Cells passing cluster growth threshold

(c) Final reconstructed topo-clusters
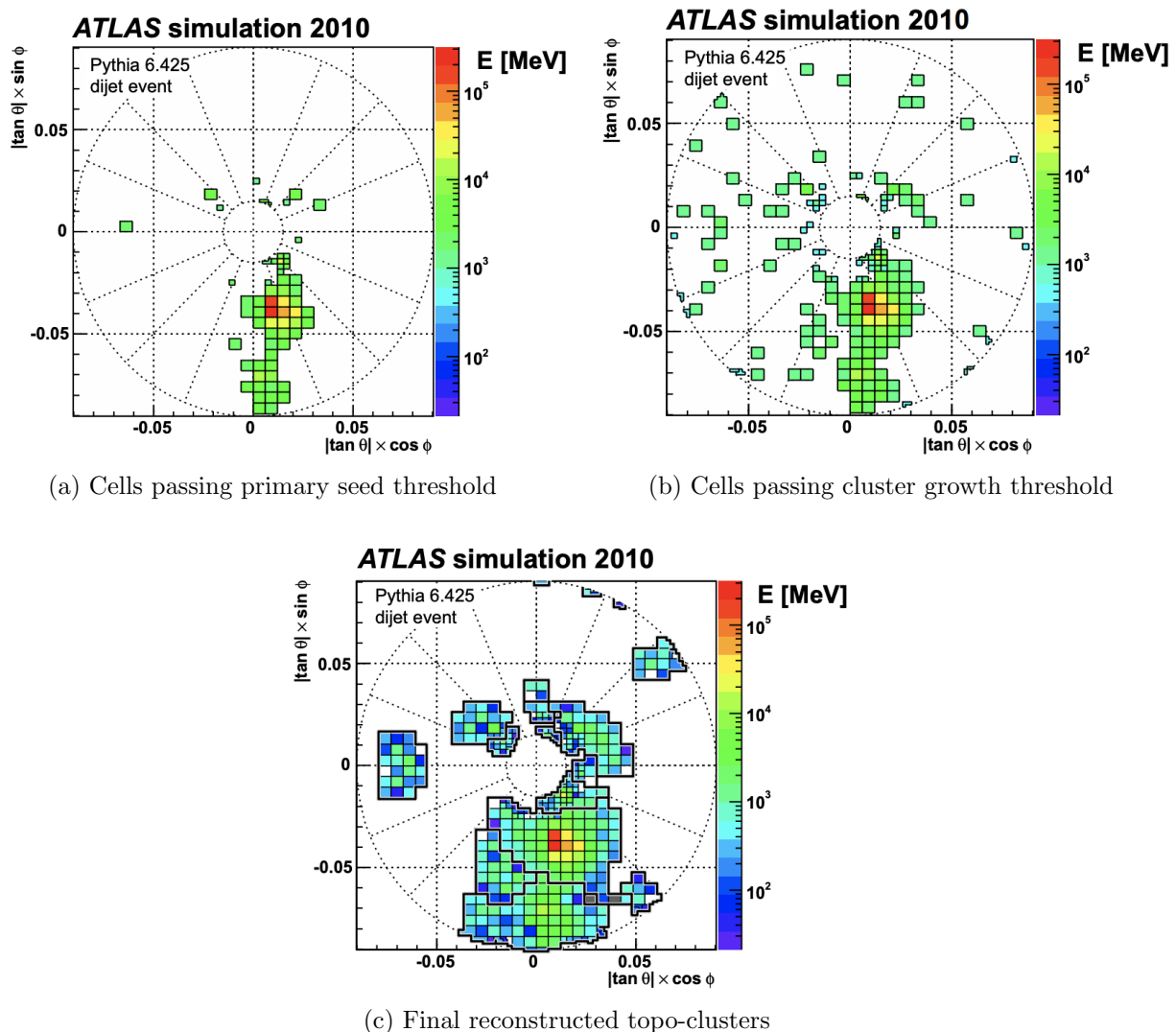
Figure 4.1: Stages of topo-cluster formation corresponding to each threshold. In (a), proto-clusters are seeded from cells with adequate signal significance $\varsigma_{\text{cell}}^{\text{EM}}$. The clusters are further merged and split in (b) following a predefined cluster growth threshold. The process stops in (c) when all sufficiently significant signal hits have been matched to a cluster [74].

4.2 Jets

Quarks, gluons and other hadrons with non-neutral color charge cannot be observed individually due to QCD color confinement, which forces a non-color-neutral hadron to

almost immediately undergo hadronization, producing a collimated cone of color-neutral hadrons defined as a jet. Jet signals can be used to reconstruct and indirectly observe the quarks or gluons from which the jet originated in the original hard-scattering process.

4.2.1   Jet reconstruction

The ATLAS jet reconstruction pipeline is largely carried out using a particle flow (PFlow) algorithm combined with an anti-k_t jet clustering algorithm. The PFlow algorithm [75] utilizes topo-clusters along with information from both the calorimeter systems and the ID in order to make use of the tracker system's advantages in low-energy momentum resolution and angular resolution. First, the energy from charged particles is removed from the calorimeter topo-clusters; then, it is replaced by particle objects created using the remaining energy in the calorimeter and tracks matched to topo-clusters. The ensemble of "particle flow objects" and corresponding matched tracks are used as inputs for the iterative anti-k_t algorithm [76].

The main components of the anti-k_t algorithm involve the distance d_{ij} between two jet candidates i and j, and the distance d_{iB} between the harder jet candidate of the two (defined as i) and the beamline B. If $d_{ij} < d_{iB}$, then the two jet candidates are combined and returned to the pool of candidates; otherwise, jet candidate i is considered a jet and removed from the pool. The distance d_{ij} is inversely proportional to a predefined radius parameter ΔR in order to control reconstruction quality for small-R and large-R jets. This analysis uses $\Delta R = 0.4$ to better handle heavily collimated small-R jets resulting from parton showers.

The anti-k_t jets so far have only been reconstructed at the EM level and need to be calibrated to match the energy scale of jets reconstructed at particle level. This is done via a MC-based jet energy scale (JES) calibration sequence, along with further calibrations

38

to account for pile-up effects and energy leakage. The full JES calibration sequence is shown in Figure 4.2. All calibrations except origin correction are applied to the jet's four-momentum i.e. jet p_T, energy and mass. Afterwards, a jet energy resolution (JER) [77] calibration step is carried out in a similar manner to JES to match the resolution of jets in dijet events. To further suppress pile-up effects, a neural-network based jet vertex tagger (NNJvt) discriminant was developed based on the previous jet vertex tagger (JVT) algorithm [73] and applied to low-p_T reconstructed jets.
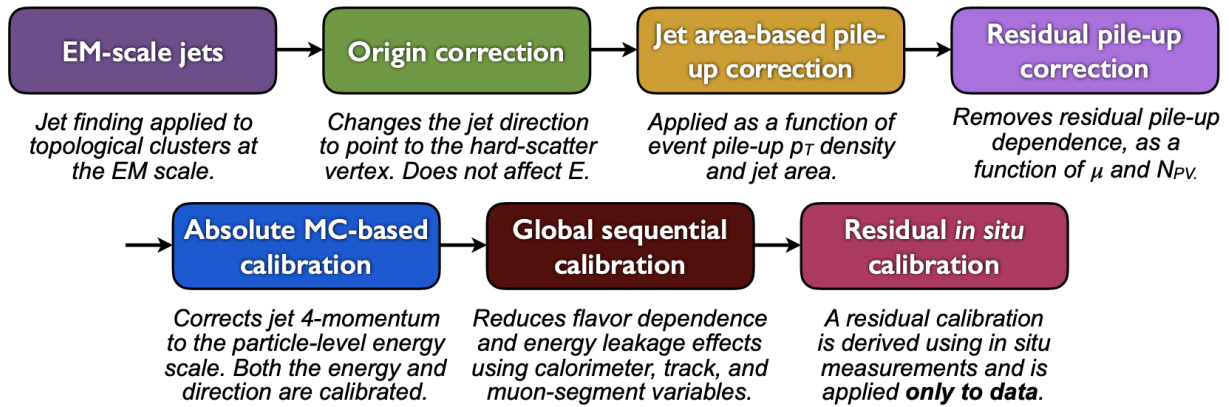
Figure 4.2: Jet energy scale calibration sequence for EM-scale jets [78].

4.2.2 Flavor tagging

Identifying and classifying hadronic jets are important tasks for ATLAS physics, for example analyses involving Higgs decays $H \to b\bar{b}$ or top quarks. Flavor tagging or b-tagging is the process of identifying jets containing b-hadrons, c-hadrons, light-hadrons (uds-hadrons) or jets from hadronically decaying τ leptons. Distinguishing b-jets is possible due to their characteristically long lifetime ($\tau \approx 1.5$ ps), displaced secondary decay vertex and high decay multiplicity.

Usage of b-tagging in this analysis is done via five operating points (OPs), corresponding

to 65%, 70%, 77%, 85% and 90% b-jet tagging efficiency ε_b in simulated $t\bar{t}$ events, in order from the tightest to loosest discriminant cut point. The OPs are defined by placing selections on the tagger output to provide a predefined ε_b level; the selection cuts act as a variable trade-off between b-tagging efficiency and b-jet purity i.e. c- or light-jet rejection. For this analysis, a jet is considered b-tagged if it passes the 85% OP. The b-tagged jet is then assigned a pseudo-continuous b-tagging (PCBT) score, which quantifies a jet's ability to satisfy different OPs. The score can take integer values between 1 and 6, where a score of 6 is assigned to jets passing all OP thresholds; a score of 2 for jets that pass only the tightest OP (90%); and a score of 1 for jets that pass no OP. A value of -1 is also defined for any jet that does not satisfy b-tagging criteria. Since the targeted $t\bar{t}t\bar{t}$ final states contain at least four b-hadrons from top and W decays, a b-tagging OP of 85% is used to maintain high purity during b-tagged jet selections in the signal region.

GN2 b-tagging algorithm

For this analysis, b-jets are identified and tagged with the GN2v01 b-tagger [79]. The GN2 algorithm uses a Transformer-based model [80] modified to incorporate domain knowledge and additional auxiliary physics objectives: grouping tracks with a common vertex and predicting the underlying physics process for a track. The network structure is shown in Figure 4.3. The GN2 b-tagger form the input vector by concatenating 2 jet variables and 19 track reconstruction variables (for up to 40 tracks), normalized to zero mean and unit variance. The output consists of a track-pairing output layer of size 2, a track origin classification layer of 7 categories, and a jet classification layer of size 4 for the probability of each jet being a b-, c-, light- or τ-jet respectively. For b-tagging purpose, a discriminant is
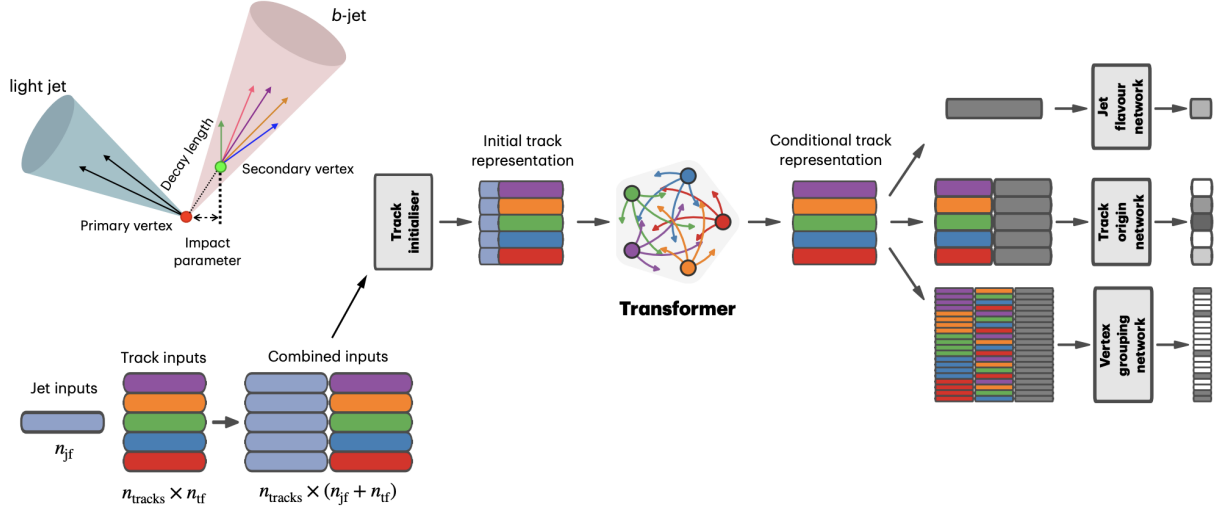
Figure 4.3: Overview of the GN2 architecture. The number of jet and track features are represented by n_{jf} and n_{tf} respectively. The global jet representation and track embeddings output by the Transformer encoder are used as inputs for three task-specific networks [79].

defined using these four outputs

$$D_b = \ln \left(\frac{p_b}{f_c p_c + f_\tau p_\tau + (1 - f_c - f_\tau) p_{\mathrm{light}}} \right) \tag{4.1}$$

where p_x is the probability of the jet being an x-jet as predicted by GN2, and f_c, f_τ are tunable free parameters controlling balance between c- and light-jet rejection.

Simulated SM $t\bar{t}$ and BSM Z' events from pp collisions were used as training and evaluation samples. In order to minimize bias, both b- and light-jet samples are re-sampled to match c-jet distributions. Figure 4.4 shows the performance of GN2 compared to the previous convolutional neural network-based standard b-tagging algorithm DL1d, in terms of c-, light- and τ-jet rejection as a function of b-tagging efficiency. The network gives a factor of 1.5-4 improvement in experimental applications compared to DL1d [79], without dependence on the choice of MC event generator or inputs from low-level flavor tagging algorithm.

41
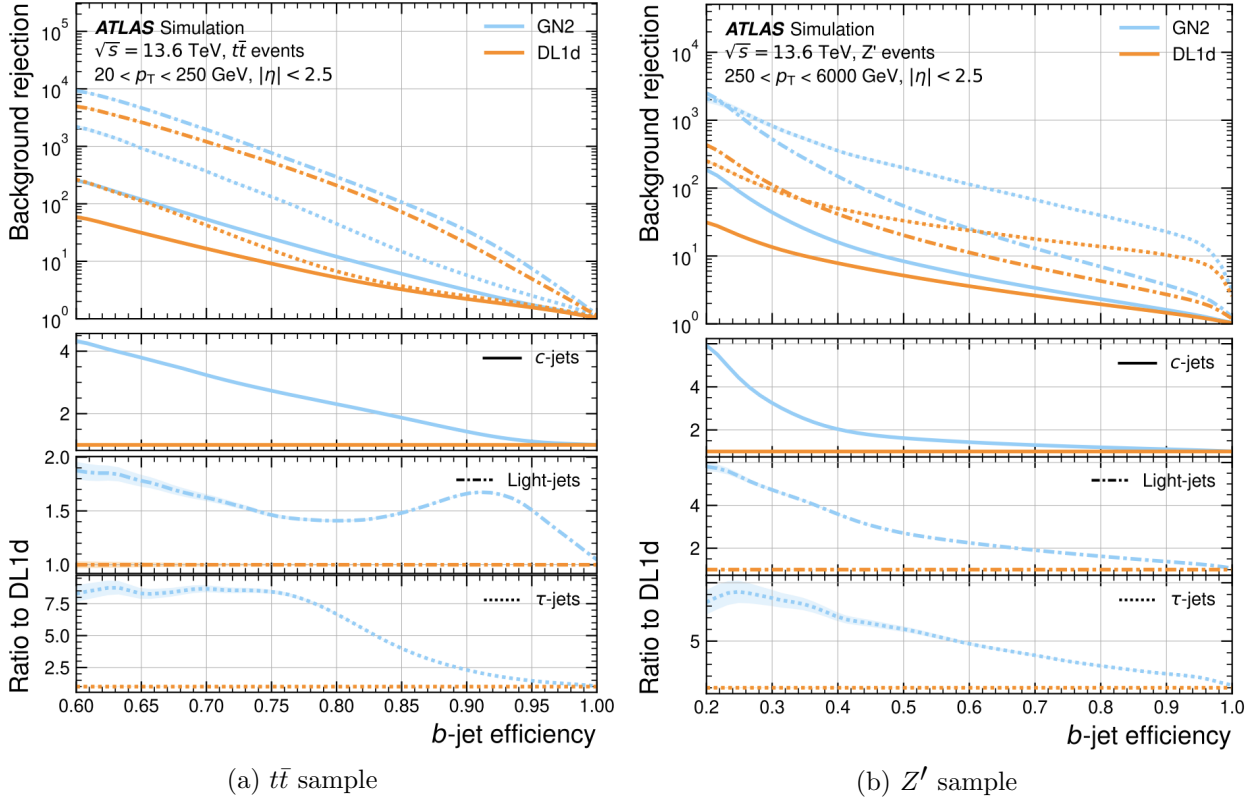
Figure 4.4: The c-, light- and τ-jet rejection rate as a function of b-tagging efficiency for GN2 and DL1d using (a) jets in the $t\bar{t}$ sample, and (b) jets in the Z' sample. The performance ratios of GN2 to DL1d are shown in the bottom panels [79].

Efficiency calibration

Due to imperfect description of detector response and physics modeling effects in simulation, the b-tagging efficiency predicted by MC simulation $\varepsilon_b^{\mathrm{sim}}$ requires a correction factor to match the efficiency measured in collision data $\varepsilon_b^{\mathrm{data}}$. The correction scale factors (SFs) are defined as $\mathrm{SF} = \varepsilon_b^{\mathrm{data}}/\varepsilon_b^{\mathrm{sim}}$ and are determined by data-to-MC calibration using samples enriched in dileptonic $t\bar{t}$ decays [81]. The resulting SFs are applied to MC simulated jets individually.

4.3 Leptons

Lepton reconstruction in ATLAS involves electron and muon reconstruction since tau decays quickly, and depending on decay mode can be reconstructed using either jets or light leptons. Leptons can be classified into two categories: prompt leptons resulting from heavy particle decays and non-prompt leptons resulting from detector or reconstruction effects, or from heavy-flavor hadron decays.

4.3.1 Electrons

Electrons leave energy signature in the detector by interacting with the detector materials and losing energy in the form of bremsstrahlung photons. A bremsstrahlung photon can produce an electron-positron pair which can itself deposit signals in the detector, creating a cascade of particles that can leave multiple of either tracks in the ID or EM showers in the calorimeters, all of which are considered part of the same EM topo-cluster. Electron signal signature has three characteristic components: localized energy deposits in the calorimeters, multiple tracks in the ID and compatibility between the above tracks and energy clusters in the $\eta \times \phi$ plane [82]. Electron reconstruction in ATLAS follows these steps accordingly.

Seed-cluster reconstruction and track reconstruction are performed sequentially in accordance with the iterative topo-clustering algorithm and track reconstruction method described in section 4.1. The seed-cluster and GSF-refitted track candidate not associated with a conversion vertex are matched to form an electron candidate. The cluster energy is then calibrated using multivariate techniques on data and simulation to match the original electron energy.

Electron identification

Additional LH-based identification selections using ID and EM calorimeter information are implemented to further improve the purity of reconstructed electrons in the $|\eta| < 2.47$ region of the detector [82]. The electron LH function is built with the signal being prompt electrons and background being objects with similar signature to prompt electrons i.e. hadronic jet deposits, photon conversions or heavy-flavor hadron decays. Three identification OPs are defined for physics analyses: *Loose*, *Medium* and *Tight*, optimized for 9 bins in $|\eta|$ and 12 bins in E_{T} with each OP corresponding to a fixed efficiency requirement for each bin. For typical EW processes, the target efficiencies for *Loose*, *Medium* and *Tight* start at 93%, 88% and 80% respectively and increase with E_{T}. Similar to b-tagging OPs, the electron identification OPs represent a trade-off in signal efficiency and background rejection. The electron efficiency are estimated using tag-and-probe method on samples of $J/\Psi \to ee$ and $Z \to ee$ [82].

Electron isolation

A characteristic distinction between prompt electrons and electrons from background processes is the relative lack of activity in both the ID and calorimeters within an $\Delta\eta \times \Delta\phi$ area surrounding the reconstruction candidate. Calorimeter-based and track-based electron isolation variables [82] are defined to quantify the amount of activity around the electron candidate using topo-clusters and reconstructed tracks respectively.

Calorimeter-based isolation variables $E_{\mathrm{T}}^{\mathrm{cone}XX}$ are computed by first summing the energy of topo-clusters with barycenters falling within a cone of radius $\Delta R = \sqrt{(\Delta\eta)^2 + (\Delta\phi)^2} = XX/100$ around the direction of the electron candidate. The final isolation variables are

obtained by subtracting from the sum the energy belonging to the candidate electron at the core of the cone, then applying corrections for pile-up effects and energy leakage outside of the core. Similar to calorimeter-based variables, track-based isolation variables $p_{\mathrm{T}}^{\mathrm{varcone}XX}$ are calculated by summing all track p_{T} within a cone of radius ΔR around the electron candidate, minus the candidate's contribution. The cone radius is variable as a function of p_{T} and is described as

$$\Delta R \equiv \min\left(\frac{10}{p_{\mathrm{T}}}, \Delta R_{\max}\right), \tag{4.2}$$

where p_{T} is expressed in GeV and $\Delta R_{\max}$ is the maximum cone size, defined to account for closer proximity of decay products to the electron in high-momentum heavy particle decays. Four isolation operating points are implemented to satisfy specific needs by physics analyses: *Loose*, *Tight*, *HighPtCaloOnly* and *Gradient* [82].

Electron charge misidentification

Charge misidentification is a crucial irreducible background, particularly for analyses with electron charge selection criteria. Electron charge is determined by the curvature of the associated reconstructed track, and misidentification of charge can occur via either an incorrect curvature measurement or an incorrectly matched track. Inaccurate measurement is more likely for high energy electrons due to the small curvature in track trajectories at high p_{T}, while track matching error usually results from bremsstrahlung pair-production generating secondary tracks in close proximity [82]. Suppression of this background is assisted via a boosted decision tree discriminant named the Electron Charge ID Selector (ECIDS) [83]. The addition of ECIDS removed 90% of electrons with incorrect charge while selecting 98%

1025 of electrons with correct charge from electrons in $Z \to ee$ events satisfying $Medium/Tight$

1026 identification and $Tight$ isolation criteria.

4.3.2   Muons

1028 Muons act as minimum-ionizing particles, leaving tracks in the MS or characteristics

1029 energy deposits in the calorimeter and can be reconstructed globally using information from

1030 the ID, MS and calorimeters. Five reconstruction strategies corresponding to five muon

1031 types [84] are utilized in ATLAS:

1032 • Combined (CB): the primary ATLAS muon reconstruction method. Combined muons

1033 are first reconstructed using MS tracks then extrapolated to include ID tracks (outside-

1034 in strategy). A global combined track fit is performed on both MS and ID tracks.

1035 • Inside-out combined (IO): complementary to CB reconstruction. IO muon tracks are

1036 extrapolated from ID to MS, then fitted with MS hits and calorimeter energy loss in a

1037 combined track fit.

1038 • MS extrapolated (ME): ME muons are defined as muons with a MS track that cannot

1039 be matched to an ID track using CB reconstruction. ME muons allow extension of

1040 muon reconstruction acceptance to regions not covered by the ID $(2.5 < |\eta| < 2.7)$

1041 • Segment-tagged (ST): ST muons are defined as a successfully matched ID track that

1042 satisfies tight angular matching criteria to at least one reconstructed MDT or CSC

1043 segment when extrapolated to the MS. MS reconstruction is used primarily when

1044 muons only crossed one layer of MS chambers.

1045 • Calorimeter-tagged (CT): CT muons are defined as an ID track that can be matched to

energy deposits consistent with those of a minimum-ionizing particle when extrapolated

through the calorimeter. CT reconstruction extends acceptance range to regions in the

MS with sparse instrumentation ($|\eta| < 0.1$) with a higher p_T threshold of 5 GeV,

compared to the 2 GeV threshold used by other muon reconstruction algorithms due

to large background contamination at the low p_T range of $15 < p_\mathrm{T} < 100$ GeV [85].

Muon identification

Reconstructed muons are further filtered by identification criteria to select for high-quality prompt muons. Requirements include number of hits in the MS and ID, track fit properties and compatibility between measurements of the two systems. Three standard OPs (*Loose*, *Medium*, *Tight*) are defined to better match the needs of different physics analyses concerning prompt muon p_T resolution, identification efficiency and non-prompt muon rejection. The default identification OP for ATLAS physics is *Medium* which provides efficiency and purity suitable for a wide range of analyses while minimizing systematic uncertainties [84].

Muon isolation

Muons from heavy particle decays are often produced in an isolated manner compared to muons from semileptonic decays, and is therefore an important tool for background rejection in many physics analyses. Muon isolation strategies are similar to that of electron in section 4.3.1, with track-based and calorimeter-based isolation variables. Seven isolation OPs are defined using either or both types of isolation variables [84].

4.4 Missing transverse momentum

Collisions at the LHC happen along the z-axis of the ATLAS coordination system between two particle beam of equal center-of-mass energy. By conservation of momentum, the sum of transverse momenta of outgoing particles should be zero. A discrepancy between measured momentum and zero would then suggest the presence of undetectable particles, which would consist of either SM neutrinos or some unknown BSM particles, making missing transverse momentum ($E_{\mathrm{T}}^{\mathrm{miss}}$) an important observable to reconstruct.

Reconstructing $E_{\mathrm{T}}^{\mathrm{miss}}$ utilizes information from fully reconstructed leptons, photons, jets and other matched track-vertex objects not associated with a prompt object (soft signals), defined with respect to the $x(y)$-axis as

$$E_{x(y)}^{\mathrm{miss}} = - \sum_{i \in \{\text{hard objects}\}} p_{x(y),i} - \sum_{j \in \{\text{soft signals}\}} p_{x(y),j}, \tag{4.3}$$

where $p_{x(y)}$ is the $x(y)$-component of p_{T} for each particle [86]. The following observables can then be defined:

$$
\begin{aligned}
\mathbf{E}_{\mathrm{T}}^{\mathrm{miss}} &= (E_x^{\mathrm{miss}}, E_y^{\mathrm{miss}}), \\
E_{\mathrm{T}}^{\mathrm{miss}} &= |\mathbf{E}_{\mathrm{T}}^{\mathrm{miss}}| = \sqrt{(E_x^{\mathrm{miss}})^2 + (E_y^{\mathrm{miss}})^2}, \\
\phi^{\mathrm{miss}} &= \tan^{-1}(E_y^{\mathrm{miss}}/E_x^{\mathrm{miss}}),
\end{aligned}
\tag{4.4}
$$

where E_T^{miss} represents the magnitude of the missing transverse energy vector $\mathbf{E}_T^{\text{miss}}$, and ϕ^{miss} its direction in the transverse plane. The vectorial sum $\mathbf{E}_T^{\text{miss}}$ can be broken down into

$$
\mathbf{E}_T^{\text{miss}} = - \underbrace{\sum_{\substack{\text{selected} \\ \text{electrons}}} \mathbf{p}_T^e - \sum_{\substack{\text{selected} \\ \text{muons}}} \mathbf{p}_T^\mu - \sum_{\substack{\text{accepted} \\ \text{photons}}} \mathbf{p}_T^\gamma - \sum_{\substack{\text{accepted} \\ \tau\text{-leptons}}} \mathbf{p}_T^\tau - \sum_{\substack{\text{accepted} \\ \text{jets}}} \mathbf{p}_T^{\text{jet}}}_{\text{hard term}} - \underbrace{\sum_{\substack{\text{unused} \\ \text{tracks}}} \mathbf{p}_T^{\text{track}}}_{\text{soft term}}.
$$
(4.5)

Two OPs are defined for E_T^{miss}, *Loose* and *Tight*, with selections on jet p_T and JVT criteria [87]. The *Tight* OP is used in this analysis; *Tight* reduces pile-up dependence of E_T^{miss} by removing the phase space region containing more pile-up than hard-scatter jets, at the expense of resolution and scale at low pile-up,

4.5 Overlap removal

Since different objects are reconstructed independently, it is possible for the same detector signals to be used to reconstruct multiple objects. An overlap removal strategy is implemented to resolve ambiguities; the overlap removal process for this analysis applies selections in Table 4.1 sequentially, from top to bottom.

Table 4.1: Overlap removal process for this analysis, applied sequentially from top to bottom.

Remove	Keep	Matching criteria
Electron	Electron	Shared ID track, $p_{T,1}^e < p_{T,2}^e$
Muon	Electron	Shared ID track, CT muon
Electron	Muon	Shared ID track
Jet	Electron	$\Delta R < 0.2$
Electron	Jet	$\Delta R < 0.4$
Jet	Muon	($\Delta R < 0.2$ or ghost-associated) & $N_{\text{track}} < 3$
Muon	Jet	$\Delta R < \min(0.4, 0.04 + 10\text{GeV}/p_T^\mu)$

Chapter 5. Data & Simulated Samples

5.1 Data samples

Data samples used in this analysis were collected by the ATLAS detector during Run 2 data-taking campaign between 2015-2018. The samples contain pp collisions at center-of-mass energy of $\sqrt{s} = 13$ TeV with 25 ns bunch-spacing, which corresponds to an integrated luminosity of $140\,\mathrm{fb}^{-1}$ with an uncertainty of 0.83% [55]. The HLT trigger strategy is similar to that of previous $t\bar{t}t\bar{t}$ observation analysis [10] and include single lepton and dilepton triggers. Calibration for di-muon and electron-muon triggers were not ready for the samples used in this analysis, and are therefore not included. Events are also required to contain at least one lepton matched to the corresponding object firing the trigger. Triggers used are summarized in Table 5.1.

5.2 Monte Carlo samples

Monte Carlo simulated samples are used to estimate signal acceptance before unblinding, profile the physics background for the analysis and to study object optimizations. Simulated samples for this analysis use are generated from ATLAS generalized MC20a/d/e samples for Run 2, using full detector simulation (FS) and fast simulation (AF3) to simulate detector response. MC samples used and simulation processes are summarized in Table 5.2

Table 5.1: Summary of all HLT triggers used in this analysis. Events are required to pass at least one trigger.

Trigger	Data period			
	2015	2016	2017	2018
Single electron triggers				
`HLT_e24_lhmedium_L1EM20VH`	✓	-	-	-
`HLT_e60_lhmedium`	✓	-	-	-
`HLT_e120_lhloose`	✓	-	-	-
`HLT_e26_lhtight_nod0_ivarloose`	-	✓	✓	✓
`HLT_e60_lhmedium_nod0`	-	✓	✓	✓
`HLT_e140_lhloose_nod0`	-	✓	✓	✓
Di-electron triggers				
`HLT_2e12_lhloose_L12EM10VH`	✓	-	-	-
`HLT_2e17_lhvloose_nod0`	-	✓	-	-
`HLT_2e24_lhvloose_nod0`	-	-	✓	✓
`HLT_2e17_lhvloose_nod0_L12EM15VHI`	-	-	-	✓
Single muon trigger				
`HLT_mu20_iloose_L1MU15`	✓	-	-	-
`HLT_mu40`	✓	-	-	-
`HLT_mu26_ivarmedium`	-	✓	✓	✓
`HLT_mu50`	-	✓	✓	✓

5.2.1 $t\bar{t}Z'$ signal samples

Signal $t\bar{t}Z'$ samples were generated based on the simplified top-philic resonance model in section 2.2.1 where a color singlet vector resonance couples strongly to only top and antitop. Six Z' mass points were utilized for the generation of the signal sample: 1000, 1250, 1500, 2000, 2500 and 3000 GeV. The top-Z' coupling c_t is chosen to be 1 for a narrow resonance peak, and the chirality angle θ is chosen to be $\pi/4$ to suppress loop production of Z'. The samples were then generated with MADGRAPH5_AMC@NLO v.3.5.0 [88] at LO with the NNPDF3.1LO [89] PDF set interfaced with PYTHIA8 [90] using A14 tune and NNPDF2.3lo PDF set for parton showering and hadronization. The resonance width is calculated to be

Table 5.2: Summary of all Monte-Carlo samples used in this analysis. V refers to an EW $(W^\pm/Z/\gamma^*)$ or Higgs boson. Matrix element (ME) order refers to the order in QCD of the perturbative calculation. Tune refers to the underlying-event tune of the parton shower (PS) generator.

Process	ME Generator	ME Order	ME PDF	PS	Tune	Sim.
Signals						
$t\bar{t}Z'$	MadGraph5_aMC@NLO	LO	NNPDF3.1LO	Pythia8	A14	FS
$t\bar{t}t\bar{t}$ **and** $t\bar{t}t$						
$t\bar{t}t\bar{t}$	MadGraph5_aMC@NLO	NLO	NNPDF3.0nlo	Pythia8	A14	AF3
	MadGraph5_aMC@NLO	NLO	MMHT2014 LO	Herwig7	H7-UE-MMHT	AF3
	Sherpa	NLO	NNPDF3.0nnlo	Herwig7	Sherpa	FS
$t\bar{t}t$	MadGraph5_aMC@NLO	LO	NNPDF2.3lo	Pythia8	A14	AF3
$t\bar{t}V$						
$t\bar{t}H$	PowhegBox v2	NLO	NNPDF3.0nlo	Pythia8	A14	FS
	PowhegBox v2	NLO	NNPDF3.0nlo	Herwig7	H7.2-Default	FS
$t\bar{t}(Z/\gamma^*)$	MadGraph5_aMC@NLO	NLO	NNPDF3.0nlo	Pythia8	A14	FS
	Sherpa	NLO	NNPDF3.0nnlo	Sherpa	Sherpa	FS
$t\bar{t}W$	Sherpa	NLO	NNPDF3.0nnlo	Sherpa	Sherpa	FS
	Sherpa	LO	NNPDF3.0nnlo	Sherpa	Sherpa	FS
$t\bar{t}$ **and Single-Top**						
$t\bar{t}$	PowhegBox v2	NLO	NNPDF3.0nlo	Pythia8	A14	FS
tW	PowhegBox v2	NLO	NNPDF3.0nlo	Pythia8	A14	FS
$t(q)b$	PowhegBox v2	NLO	NNPDF3.0nlo (s)	Pythia8	A14	FS
			NNPDF3.0nlo 4f (t)			FS
tWZ	MadGraph5_aMC@NLO	NLO	NNPDF3.0nlo	Pythia8	A14	FS
tZ	MadGraph5_aMC@NLO	LO	NNPDF3.0nlo 4f	Pythia8	A14	FS
$t\bar{t}VV$						
$t\bar{t}WW$	MadGraph5_aMC@NLO	LO	NNPDF3.0nlo	Pythia8	A14	FS
$t\bar{t}WZ$	MadGraph	LO	NNPDF3.0nlo	Pythia8	A14	AF3
$t\bar{t}HH$	MadGraph	LO	NNPDF3.0nlo	Pythia8	A14	AF3
$t\bar{t}WH$	MadGraph	LO	NNPDF3.0nlo	Pythia8	A14	AF3
$t\bar{t}ZZ$	MadGraph	LO	NNPDF3.0nlo	Pythia8	A14	AF3
$V(VV)$**+jets and** VH						
V+jets	Sherpa	NLO	NNPDF3.0nnlo	Sherpa	Sherpa	FS
VV+jets	Sherpa	NLO	NNPDF3.0nnlo	Sherpa	Sherpa	FS
		LO $(gg \to VV)$				FS
VVV+jets	Sherpa	NLO	NNPDF3.0nnlo	Sherpa	Sherpa	FS
VH	PowhegBox v2	NLO	NNPDF3.0aznlo	Pythia8	A14	FS

1115 4% for $c_t = 1$.

5.2.2 Background samples

SM $t\bar{t}t\bar{t}$ background

1118 The nominal SM $t\bar{t}t\bar{t}$ sample was generated with MADGRAPH5_AMC@NLO [88] at NLO

1119 in QCD with the `NNPDF3.0nlo` [89] PDF set and interfaced with PYTHIA8.230 [90] using A14

1120 tune [91]. Decays for top quarks are simulated at LO with MADSPIN [92, 93] to preserve

1121 spin information, while decays for b- and c-hadrons are simulated with EVTGEN v1.6.0

1122 [94]. The renormalization and factorization scales μ_R and μ_F are set to $\sqrt{m^2 + p_\mathrm{T}^2}/4$, which

1123 represents the sum of transverse mass of all particles generated from the ME calculation [95].

1124 The ATLAS detector response was simulated with AF3. Additional auxiliary $t\bar{t}t\bar{t}$ samples

1125 are also generated to evaluate the impact of generator and PS uncertainties as shown in 5.2.

$t\bar{t}W$ background

1127 Nominal $t\bar{t}W$ sample was generated using SHERPA v2.2.10 [96] at NLO in QCD with

1128 the `NNPDF3.0nnlo` [89] PDF with up to one extra parton at NLO and two at LO, which

1129 are matched and merged with SHERPA PS based on Catani-Seymour dipole factorization

1130 [97] using the MEPS@NLO prescription [98–101] and a merging scale of 30 GeV. Higher-

1131 order ME corrections are provided in QCD by the OpenLoops 2 library [102–104] and in

1132 EW from $\mathcal{O}(\alpha^3) + \mathcal{O}(\alpha_S^2\alpha^2)$ (LO3 & NLO2) via two sets of internal event weights. An

1133 alternative sample with only EW corrections at LO from $\mathcal{O}(\alpha_S\alpha^3)$ (NLO3) diagrams were

1134 also simulated with the same settings.

$t\bar{t}(Z/\gamma^*)$ background

Nominal $t\bar{t}(Z/\gamma^*)$ samples were generated separately for different ranges of dilepton invariant mass $m_{\ell\ell}$ to account for on-shell and off-shell Z/γ^* production. Sample for $m_{\ell\ell}$ between 1 and 5 GeV was produced using MadGraph5_aMC@NLO [88] at NLO with the NNPDF3.0nlo [89] PDF set, interfaced with Pythia8.230 [90] using A14 tune [91] and NNPDF2.3lo PDF set. Sample for $m_{\ell\ell} < 5$ GeV was produced with Sherpa v2.2.10 [96] at NLO using NNPDF3.0nnlo PDF set. To account for generator uncertainty, an alternative $m_{\ell\ell} > 5$ GeV sample was generated with identical settings to the low $m_{\ell\ell}$ sample. The ATLAS detector response was simulated with full detector simulation (FS).

Chapter 6. Analysis Strategy

6.1 Event selection

Events for the analysis first are preselected following a list of criteria to optimize for event quality and background rejection. The following criteria are applied sequentially from top to bottom along with cleaning and veto cuts

1. **Good Run List (GRL)**: data events must be part of a predefined list of suitable runs and luminosity blocks [105].

2. **Primary vertex**: events must have at least one reconstructed vertex matched to 2 or more associated tracks with $p_T > 500$ MeV.

3. **Trigger**: events must be selected by at least one trigger in Table 5.1.

4. **Kinematic selection**: events must have exactly two *Tight* leptons with the same electric charge, or at lease three *Tight* leptons of any charge. The leading lepton must have $p_T > 28$ GeV, and all leptons must satisfy $p_T > 15$ GeV.

Events are separated into two channels based on the number of leptons: same-sign di-lepton (SS2L) for events with exactly two leptons of the same charge, or multilepton (ML) for events with three or more leptons. The channels are further separated into regions defined in section 6.2 to prepare for analysis.

Additional selections are applied based on the lepton flavors present. In the SS2L channel, if both leptons are electrons, the invariant mass m_{ll} must satisfy $m_{ll} < 81$ GeV and $m_{ll} > 101$ GeV to suppress background involving Z-bosons. In the ML channel, the same criteria must be satisfied for every opposite-sign same-flavor pair of leptons in an event.

6.1.1 Object definition

Table 6.1 shows the selections used in this analysis. Each selection comes with associated

calibration scale factors (SFs) to account for discrepancies between data and MC simulation,

and are applied multiplicatively to MC event weights.

Table 6.1: Summary of object selection criteria used in this analysis. ℓ_0 refers to the leading lepton in the event.

Selection	Electrons	Muons	Jets
p_T [GeV]	> 15 $p_\mathrm{T}(\ell_0) > 28$	> 15	> 20
$\|\eta\|$	$1.52 \leq \|\eta\| < 2.47$ < 1.37	< 2.5	< 2.5
Identification	*TightLH* pass ECIDS ($ee/e\mu$)	*Medium*	NNJvt *FixedEffPt* ($p_\mathrm{T} < 60$, $\|\eta\| < 2.4$)
Isolation	*Tight_VarRad*	*PflowTight_VarRad*	
Track-vertex assoc. $\|d_0^{\mathrm{BL}}(\sigma)\|$ $\|\Delta z_0^{\mathrm{BL}} \sin\theta\|$ [mm]	< 5 < 0.5	< 3 < 0.5	

6.1.2 Event categorization

Simulated events are categorized using truth information of leptons (e/μ) and their orig-

inating MC particle (mother-particle). Each lepton can be classified as either prompt or

non-prompt, with non-prompt leptons further categorized for background estimation pur-

poses. If an event contains only prompt leptons, the event is classified as its corresponding

process. If the event contains one non-prompt lepton, the event is classified as the corre-

sponding type of the non-prompt lepton. If the event contains more than one non-prompt

lepton, the event is classified as other.

- **Prompt**: if the lepton originates from $W/Z/H$ boson decays, or from a mother-particle created by a final state photon.

- **Non-prompt**:

  - **Charge-flip (e only)**: if the reconstructed charge of the lepton differs from that of the first mother-particle.

  - **Material conversion (e only)**: if the lepton originated from a photon conversion and the mother-particle is an isolated prompt photon, non-isolated final state photon, or heavy boson.

  - **γ^*-conversion (e only)**: if the lepton originated from a photon conversion and the mother-particle is a background electron.

  - **Heavy flavor decay**: if the lepton originated from a b- or c-hadron.

  - **Fake**: if the lepton originated from a light- or s-hadron, or if the truth type of the lepton is hadron.

  - **Other**: any lepton that does not belong to one of the above categories.

6.2   Analysis regions

Events are selected and categorized into analysis regions belonging to one of two types: control regions (CRs) enriched in background events, and signal regions (SRs) enriched in signal events. This allows for the examination and control of backgrounds and systematic uncertainties, as well as study of signal sensitivities. The signal is then extracted from the SRs with a profile LH fit using all regions. The full selection criteria for each region are summarized in Table 6.2.

57

Table 6.2: Definitions of signal, control and validation regions (VR) used in this analysis. N_{jets} and N_b refers to the number of jets and number of b-tagged jets respectively. ℓ_1 refers to the leading lepton, ℓ_2 refers to the subleading lepton and so on. H_{T} refers to the p_{T} scalar sum of all leptons and jets in the event. $m_{\ell\ell}$ refers to the dilepton invariant mass, which must not coincide with the Z-boson mass range of 81-101 GeV for SS2L+3L events.

Region	Channel	N_{jets}	N_b	Other selections	Fitted variable
CR Low $m_{\gamma*}$	SS $e\ell$	$[4,6)$	≥ 1	ℓ_1/ℓ_2 is from virtual photon decay $\ell_1 + \ell_2$ not from material conversion	event yield
CR Mat. Conv.	SS $e\ell$	$[4,6)$	≥ 1	ℓ_1/ℓ_2 is from material conversion	event yield
CR HF μ	$\ell\mu\mu$	≥ 1	1	$\ell_1 + \ell_2$ not conversion candidates $100 < H_{\text{T}} < 300$ GeV $E_{\text{T}}^{\text{miss}} > 35$ GeV total charge $= \pm 1$	$p_{\text{T}}(\ell_3)$
CR HF e	$ee\ell$	≥ 1	1	$\ell_1 + \ell_2$ not conversion candidates $100 < H_{\text{T}} < 275$ GeV $E_{\text{T}}^{\text{miss}} > 35$ GeV total charge $= \pm 1$	$p_{\text{T}}(\ell_3)$
CR $t\bar{t}W^+$	SS $\ell\mu$	≥ 4	≥ 2	$\|\eta(e)\| < 1.5$ for $N_b = 2$: $H_{\text{T}} < 500$ GeV or $N_{\text{jets}} < 6$ for $N_b \geq 3$: $H_{\text{T}} < 500$ GeV total charge > 0	N_{jets}
CR $t\bar{t}W^-$	SS $\ell\mu$	≥ 4	≥ 2	$\|\eta(e)\| < 1.5$ for $N_b = 2$: $H_{\text{T}} < 500$ GeV or $N_{\text{jets}} < 6$ for $N_b \geq 3$: $H_{\text{T}} < 500$ GeV total charge < 0	N_{jets}
CR 1b(+)	SS2L+3L	≥ 4	1	$\ell_1 + \ell_2$ not from material conversion $H_{\text{T}} > 500$ GeV total charge > 0	N_{jets}
CR 1b(-)	SS2L+3L	≥ 4	1	$\ell_1 + \ell_2$ not from material conversion $H_{\text{T}} > 500$ GeV total charge < 0	N_{jets}
VR $t\bar{t}Z$	3L $\ell^\pm \ell^\mp$	≥ 4	≥ 2	$m_{\ell\ell} \in [81, 101]$ GeV	N_{jets}, $m_{\ell\ell}$
VR $t\bar{t}W$ +1b	SS2L+3L			CR $t\bar{t}W^\pm$ || CR 1b($\pm$)	N_{jets}
VR $t\bar{t}W$ +1b+SR	SS2L+3L			CR $t\bar{t}W^\pm$ || CR 1b($\pm$) || SR	N_{jets}
SR	SS2L+3L	≥ 6	≥ 2	$H_{\text{T}} > 500$ GeV $m_{\ell\ell} \notin [81, 101]$ GeV	H_{T}

6.2.1 Signal regions

All events selected for the SR must satisfy the following criteria:

- Contains 6 or more jets, with at least 2 jets b-tagged at the 85% OP.

- Scalar sum of the transverse momenta of all leptons and jets $H_\mathrm{T} > 500$ GeV.

- Dilepton invariant mass $m_{\ell\ell}$ does not coincide with the Z-boson mass range of $81 - 101$ GeV

The SR is further divided into sub-regions by the number of b-jets and leptons as shown in Table 6.3 to further study signal behavior and improve sensitivity.

Table 6.3: Definitions of SR sub-regions. Events are sorted into different sub-regions based on the number of b-tagged jets and leptons present.

| Sub-region | Selection criteria | |
	b-jets	leptons
SR 2b2l	$N_b = 2$	$N_l = 2$
SR 2b3l4l	$N_b = 2$	$N_l \geq 3$
SR 3b2l	$N_b = 3$	$N_l = 2$
SR 3b3l4l	$N_b = 3$	$N_l \geq 3$
SR 4b	$N_b \geq 4$	

6.2.2 Control regions

Control regions are defined for each background to be enriched in the targeted process, in order to maximize the background's purity and minimize contamination from other sources within the region. This helps to constrain and reduce correlation between background normalization factors in the final fit. Fit variables and selection criteria are determined via

optimization studies performed on CRs that aimed to achieve the largest discriminating power possible between the target background and other event types.

$t\bar{t}W$ background CRs

Theoretical modeling for $t\bar{t}W$ +jets background in the phase space of this analysis suffers from large uncertainties, especially at high jet multiplicities [106]. A data-driven method was employed in a similar manner to the SM $t\bar{t}t\bar{t}$ observation analysis [10] to mitigate this effect, and are described in further details in section 6.3.3. The method necessitates the definition of two groups of dedicated CRs to estimate the flavor composition and normalization of $t\bar{t}W$ +jets background: CR $t\bar{t}W$ +jets to constrain flavor composition, and CR 1b to constrain the jet multiplicity spectrum. These are further split into CR $t\bar{t}W^{\pm}$ and CR 1b($\pm$) due to the pronounced asymmetry in $t\bar{t}W$ production from pp collisions, with $t\bar{t}W^{+}$ being produced at approximately twice the rate of $t\bar{t}W^{-}$ [107].

Events in CR $t\bar{t}W^{\pm}$ are required to contain at least two b-tagged jets similar to the SR to determine the $t\bar{t}W$ normalization within an SR-related phase space. Orthogonality with SR is ensured by requiring $H_{\mathrm{T}} < 500$ GeV or $N_{\mathrm{jets}} < 6$ when $N_b = 2$, and $H_{\mathrm{T}} < 500$ GeV when $N_b \geq 3$. Events in CR 1b($\pm$) are required to have $H_{\mathrm{T}} > 500$ GeV and at least four jets to encompass events with high N_{jets}, which can be used to determine the $t\bar{t}W$ jet multiplicity spectrum for fitting $a_{0,1}$. The selection criteria also include exactly one b-tagged jet to maintain orthogonality with the SR.

Fake/non-prompt background CRs

Selection for fake/non-prompt CRs are determined using the `DFCommonAddAmbiguity` (DFCAA) variable for reconstructed leptons.

Table 6.4: List of possible assigned values for DFCAA.

DFCAA	Description
-1	No 2nd track found
0	2nd track found, no conversion found
1	Virtual photon conversion candidate
2	Material conversion candidate

Four CRs are defined for the three main types of fake/non-prompt backgrounds in the analysis - virtual photon (γ^*) conversion, photon conversion in detector material (Mat. Conv.) and heavy flavor decays (HF). The full selection criteria for fake/non-prompt CRs are shown in Table 6.2.

- **Low m_γ^***: events with an e^+e^- pair produced from a virtual photon.

  Events are selected if there are two same-sign leptons with at least one electron reconstructed as an internal conversion candidate, and neither reconstructed as a material conversion candidate.

- **Mat. Conv.**: events with an electron originating from photon conversion within the detector material.

  Events are selected if there are two same-sign leptons with at least one electron reconstructed as a material conversion candidate.

- **HF $e(\mu)$**: events with a reconstructed non-prompt lepton from semi-leptonic decays of b- and c-hadrons (heavy flavor decays).

  Events are selected if there are three leptons with at least two electrons (muons), with no lepton reconstructed as a conversion candidate.

6.3 Background estimation

Background in this analysis consist of SM processes that can result in a signal signature similar to a $t\bar{t}t\bar{t}$ SSML final state and can be divided into two types, reducible and irreducible. Reducible background consists of processes that do not result in a SSML final state physically, but are reconstructed as such due to detector and reconstruction effects. Three main types of reducible background are considered: charge misidentification (QmisID) and fake/non-prompt leptons. Fake/non-prompt lepton backgrounds are estimated using template fitting method, where MC simulations are normalized to their theoretical SM cross section via floating normalization factors (NFs) constrained by the corresponding CRs. Lepton charge misidentification background contaminates the SR with opposite-sign events, and are estimated using a data-driven method described in section 6.3.2 along with ECIDS described in section 4.3.1.

Irreducible background consists of SM processes that result in SSML final states physically with all leptons being prompt. The dominating background in the SR are SM $t\bar{t}t\bar{t}$, $t\bar{t}W$, $t\bar{t}Z$, and $t\bar{t}H$ production with smaller contributions from VV, VVV, VH and rarer processes like $t\bar{t}VV$, tWZ, tZq and $t\bar{t}t$. Most irreducible backgrounds are estimated using template fitting method, with the exception of $t\bar{t}W$ +jets background.The $t\bar{t}W$ +jets bacgkround is instead given four dedicated CRs, and estimated using a data-driven method with a fitted function parameterized in N_{jets}. All CRs and SR are included in the final profile LH fit to data.

6.3.1 Template fitting for fake/non-prompt estimation

Template fitting method is a semi-data-driven approach [106] that estimates fake/non-prompt background distributions by fitting the MC kinematic profile of background processes arising from fake/non-prompt leptons to data. Each of the four main sources of fake/non-prompt leptons is assigned a free-floating NF constrained by a CR enriched with the corresponding background resulting in four $\mathrm{NF}_{\mathrm{HF}\ e}$, $\mathrm{NF}_{\mathrm{HF}\ \mu}$, $\mathrm{NF}_{\mathrm{Mat.\ Conv.}}$ and $\mathrm{NF}_{\mathrm{Low}\ m_{\gamma*}}$. The NFs are fitted simultaneously with the signal.

6.3.2 Charge misidentification data-driven estimation

The ee and $e\mu$ channels in the SS2L region are contaminated with opposite-sign (OS) dilepton events with one misidentified charge. Charge misidentification (QmisID) largely affects electrons due to muons' precise curvature information using ID and MS measurements and low bremsstrahlung rate. The charge flip rates are significant at higher p_{T} and varies with $|\eta|$ which is proportional to the amount of detector material the electron interacted with.

The charge flip probability ϵ is estimated in this analysis with a data-driven method [108] using a sample of $Z \to e^+e^-$ events with additional constraints on the invariant mass m_{ee} to be within 10 GeV of the Z-boson mass. The Z-boson mass window is defined to be within 4σ to include most events within the peak, and is determined by fitting the m_{ee} spectrum of the two leading electrons to a Breit-Wigner function, resulting in a range of $[65.57, 113.49]$ for SS events and $[71.81, 109.89]$ for OS events. Background contamination near the peak is assumed to be uniform and subtracted using a sideband method. Since the Z-boson decay products consist of a pair of opposite-sign electrons, all same-sign electron

$_{1291}$ pairs are considered affected by charge misidentification.

$_{1292}$ Let N_{ij}^{SS} be the number of events with SS electrons with the leading electron in the

$_{1293}$ i^{th} 2D bin in $(p_{\mathrm{T}}, |\eta|)$ and the sub-leading electron in the jth bin. Assuming the QmisID

$_{1294}$ probabilities of electrons in an event are uncorrelated, N_{ij}^{SS} can be estimated as

$$N_{ij}^{\mathrm{SS}} = N_{ij}^{\mathrm{tot}} \left[\epsilon_i(1 - \epsilon_j) + \epsilon_j(1 - \epsilon_i) \right], \tag{6.1}$$

$_{1295}$ where N_{ij}^{tot} is the total number of events in the ith and j^{th} bin regardless of charge, and

$_{1296}$ $\epsilon_{i(j)}$ is the QmisID rate in the $i^{\mathrm{th}}(j^{\mathrm{th}})$ bin. Assuming N_{ij}^{SS} follows a Poisson distribution

$_{1297}$ around the expectation value $\bar{N}_{ij}^{\mathrm{SS}}$, the $(i,n)^{\mathrm{th}}$ rate ϵ can be estimated by minimizing a

$_{1298}$ negative-LLH function parameterized in p_{T} and $|\eta|$,

$$
\begin{aligned}
-\ln(\mathcal{L}(\epsilon|N_{\mathrm{SS}})) &= -\ln \prod_{ij} \frac{(N_{ij}^{\mathrm{tot}})^{N_{ij}^{\mathrm{SS}}} \cdot e^{N_{ij}^{\mathrm{tot}}}}{N_{ij}^{\mathrm{SS}}!} \\
&= -\sum_{ij} \left[N_{ij}^{\mathrm{SS}} \ln(N_{ij}^{\mathrm{tot}}(\epsilon_i(1-\epsilon_j) + \epsilon_j(1-\epsilon_i))) - N_{ij}^{\mathrm{tot}}(\epsilon_i(1-\epsilon_j) + \epsilon_j(1-\epsilon_i)) \right].
\end{aligned}
\tag{6.2}
$$

$_{1299}$ The QmisID rates are then calculated separately for SR and CRs with different electron

$_{1300}$ definitions i.e. CR Low $m_{\gamma*}$, CR Mat. Conv., CR $t\bar{t}W^{\pm}$, using events from data after

$_{1301}$ applying region-specific lepton selections and ECIDS. The events are required to satisfy

$_{1302}$ SS2L kinematic selections but contains OS electrons. The following weight is applied to OS

$_{1303}$ events to correct for misidentified SS events within the region,

$$w = \frac{\epsilon_i + \epsilon_j - 2\epsilon_i\epsilon_j}{1 - \epsilon_i - \epsilon_j + 2\epsilon_i\epsilon_j}. \tag{6.3}$$

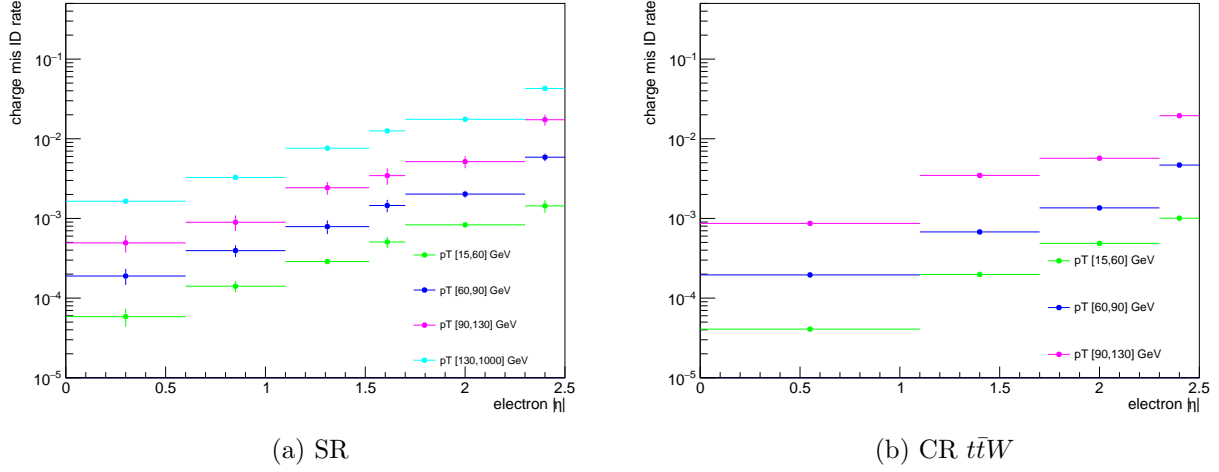The QmisID rates calculated for SR and CR $t\bar{t}W$ are shown in Figure 6.1

(a) SR   (b) CR $t\bar{t}W$

Figure 6.1: Charge flip rate calculated for SR and CR $t\bar{t}W$ in bins of $|\eta|$ and p_{T}.

The QmisID rates obtained after applying w contain a dependency on jet multiplicity and are underestimated at higher N_{jets}. This dependency affect the SR which require events with ≥ 6 jets, and is corrected by applying a correction factor $\mathrm{SF}_{i,n} = \epsilon_{i,n}/\epsilon_{i,N}$ where N is the inclusive bin containing all N_{jets} and $\epsilon_{i,n}$ is the QmisID rate obtained from Equation 6.2 in the $(i,n)^{\mathrm{th}}$ 2D bin in $(p_{\mathrm{T}}, N_{\mathrm{jets}})$. Jet multiplicity and consequently the obtained SFs are assumed to be independent of $|\eta|$.

6.3.3 $t\bar{t}W$ background data-driven estimation

Previously, the $t\bar{t}W$ background in $t\bar{t}t\bar{t}$ final state analysis was handled by assigning large ad-hoc systematic uncertainties to $t\bar{t}W$ events with 7 or more jets [12]. A semi-data-driven method [109] was shown to be effective in the SM $t\bar{t}t\bar{t}$ observation analysis [10] by improving $t\bar{t}W$ modeling, especially in the showering step and switching $t\bar{t}W$ systematic uncertainties from predominantly modeling to statistical.

The data-driven method applies correction factors obtained from a fitted function parameterized in N_{jets} to $t\bar{t}W$ MC kinematic distibutions. The QCD scaling patterns [110] can be represented by ratio of successive exclusive jet cross-sections

$$R_{(n+1)/n} = \frac{\sigma_{n+1}}{\sigma_n} = e^{-b} + \frac{\bar{n}}{n+1} = a_0 + \frac{a_1}{1+(j-4)}, \tag{6.4}$$

where $a_{0(1)}$ and b are constants, n is the number of jets in addition to the hard process, j is the inclusive number of jets, and $\bar{n}$ is the expectation value for the Poisson distribution of exclusive jet cross-section at jet multiplicity n. The $t\bar{t}W$ ME for SS2L events gives 4 jets in the hard process, so n is defined starting from the 5th jets and the inclusive number of jets $j = n + 4$. The two terms in Equation 6.4 correspond to staircase and Poisson scaling in cross section between successive jet multiplicities and are sensitive to high and low jet multiplicity events respectively [110]. The scaling pattern can then be reparameterized in a_0 and a_1 to obtain the $t\bar{t}W$ yield at $j' \equiv j + 1$ jets

$$\text{Yield}_{t\bar{t}W(j')} = \text{Yield}_{t\bar{t}W(N_{\text{jets}}=4)} \times \prod_{j=4}^{j'-1} \left(a_0 + \frac{a_1}{1+(j-4)} \right) \tag{6.5}$$

with $j \geq 4$. The $t\bar{t}W$ yield in the 4-jet bin can be represented by a NF applied to $t\bar{t}W$ MC simulation

$$\text{Yield}_{t\bar{t}W(N_{\text{jets}}=4)} = \text{NF}_{t\bar{t}W(N_{\text{jets}}=4)} \times \text{MC}_{t\bar{t}W(N_{\text{jets}}=4)}. \tag{6.6}$$

To account for the asymmetry in $t\bar{t}W^+$ and $t\bar{t}W^-$ cross-sections, $\text{NF}_{t\bar{t}W(N_{\text{jets}}=4)}$ is further split into $\text{NF}_{t\bar{t}W^\pm(N_{\text{jets}}=4)}$ assuming the scaling is the same for both processes. Both NFs are left free-floating to constrain $t\bar{t}W$ yields in the 4-jet bin within CR 1b(+) and CR 1b(-).

The final N_{jets}-parameterized function can then be represented by $\text{NF}_{t\bar{t}W(j')}$ as

$$\text{NF}_{t\bar{t}W(j')} = \left(\text{NF}_{t\bar{t}W^+(N_{\text{jets}}=4)} + \text{NF}_{t\bar{t}W^-(N_{\text{jets}}=4)}\right) \times \prod_{j=4}^{j'-1}\left(a_0 + \frac{a_1}{1+(j-4)}\right). \quad (6.7)$$

The normalization is calculated and applied separately for each sub-sample of $t\bar{t}W^+$ and $t\bar{t}W^-$ in a N_{jets} bin for $4 \leq N_{\text{jets}} < 10$. Due to small contributions in the CRs, events with $N_{\text{jets}} < 4$ and $N_{\text{jets}} \geq 10$ are not normalized with this scheme. Instead, $N_{\text{jets}} < 4$ events are fitted by propagating the normalization in the 4-jet bin without additional shape correction. The correction factor for $t\bar{t}W$ events with $N_{\text{jets}} \geq 10$ is obtained by summing up the overflow from $N_{\text{jets}} = 10$ to $N_{\text{jets}} = 12$, described as $\sum_{j'=10}^{12} \prod_{j=4}^{j'-1}\left(a_0 + \frac{a_1}{1+(j-4)}\right)$. Events with $N_{\text{jets}} \geq 13$ are negligible and are not included in the sum.

The four regions, CR $t\bar{t}W^\pm$ and CR 1b($\pm$), are constructed to fit $\text{NF}_{t\bar{t}W^\pm(N_{\text{jets}}=4))}$ and the scaling parameters $a_{0(1)}$, as well as validating the parameterization. Assuming the N_{jets} distribution of $t\bar{t}W$ is similar across bins of $N_{b\text{-jets}}$, a fitted N_{jets} distribution in CR 1b($\pm$) can be used to describe the $t\bar{t}W$ parameterization at higher N_{jets}.

Chapter 7. Systematic Uncertainties

Physics analysis inherently incurs uncertainties in the form of statistical and systematic uncertainties, depending on the source. Statistical uncertainties occur in this analysis from sample size of collected data and simulated MC samples, and from the maximizing of the LH function. Systematic uncertainties depend on identifiable sources in the analysis i.e. from detector and reconstruction effects (experimental uncertainties) or theoretical modeling (theoretical uncertainties). Systematic uncertainties are represented as nuisance parameters (NPx) in the profile LH fit. During the fit, systematic uncertainties with negligible impact on the final results can be pruned to simplify the statistical model and reduce computational complexity. This section outlines all uncertainties considered in this analysis.

7.1 Experimental uncertainties

7.1.1 Luminosity & pile-up reweighting

Uncertainty on the integrated luminosity of the 2015-2018 Run 2 data set is 0.83% [55], obtained by the LUCID-2 detector [111] for the primary luminosity measurements and complemented by the ID and calorimeters. Pile-up was modeled in MC and calibrated to data through pile-up reweighting, resulting in a set of calibration SFs and associated uncertainties.

7.1.2 Leptons

In general, calibrating MC simulations to match performance in data incurs uncertainties associated obtaining the MC-to-data calibration SFs, which are in turn propagated to observables in the analysis. The data-to-MC calibration of trigger, reconstruction, identification

Table 7.1: Summary of the experimental systematic uncertainties considered in this analysis.

Systematic uncertainty	Components
Event	
Luminosity	1
Pile-up reweighting	1
Electrons	
Trigger efficiency	1
Reconstruction efficiency[†]	1
Identification efficiency[†]	1
Isolation efficiency[†]	1
Energy scale	1
Energy resolution	1
Charge identification (ECIDS) efficiency[†]	1
Muons	
Trigger efficiency	2
Track-to-vertex association efficiency	2
Reconstruction/identification efficiency	2
Low-p_T (< 15 GeV) reconstruction/identification efficiency	2
Isolation efficiency	2
Charge-independent momentum scale	1
Charge-dependent momentum scale	4
Energy resolution (CB)	1
Energy resolution (ID & MS)[†]	2
Jets	
JES effective NP	15
JES η intercalibration	3
JES flavor composition	2
JES flavor response	1
JES pile-up	4
JES punch-through (FS/AF3)	2
JES non-closure	1
JES high-p_T single particle	1
JES b-jet response	1
JER effective NP	12
JER data/MC (FS/AF3)	2
JVT efficiency	1
GN2v01 b-tagging efficiency	85
GN2v01 c-tagging efficiency	56
GN2v01 light-tagging efficiency	42
E_T^{miss} **track-based soft terms**	
Transversal resolution	1
Longitudinal resolution	1
Longitudinal energy scale	1

[†]Not ready for the analysis, but will be included

and isolation efficiencies for electrons and muons incur associated uncertainties, with separate systematic and statistical components for those related to muons. Similarly, electron and muon energy-momentum scale and resolution are also subjected to calibration uncertainties estimated by varying the corresponding calibration quantity during simulation. Electron has an additional uncertainty related to ECIDS efficiency. Muon has additional uncertainties for charge-independent and charge-dependent momentum scale, as well as detector-specific track resolution. Systematic uncertainties for electron reconstruction, identification, isolation, ECIDS efficiencies and muon ID/MS energy resolution were not ready for the sample version used in this analysis, and are therefore not included.

7.1.3 Jets

Experimental uncertainties for jets are dominated by flavor tagging-related uncertainties, with subleading contributions from uncertainties related to JES [78], JER [77] and JVT [112] calibrations.

Jet energy scale

Uncertainties associated with JES are determined using data from LHC collisions along with MC simulated samples [78], decomposed into uncorrelated components:

- **Effective NPs**: 15 total p_T-dependent uncertainty components measured in situ, grouped based on their origin (2 detector-related, 4 modeling-related, 3 mixed, 6 statistical-related)

- η **intercalibration**: 6 total components (1 modeling-related, 4 non-closure and 1 statistical-related) associated with the correction of the forward jets' $(0.8 \leq |\eta| < 4.5)$

energy scale to that of the central jets ($|\eta| < 0.8$).

- **Flavor composition & response**: 2 components for relative quark-gluon flavor compositions in background and signal samples, and 2 components for responses to gluon-initiated versus quark-initiated jets.

- **Pile-up subtraction**: 4 components, 2 for μ (`OffsetMu`) and N_{PV} (`OffsetNPV`) modeling, 1 for residual p_{T}-dependency (`PtTerm`) and 1 for topology dependence on the per-event p_{T} density modeling (`RhoTopology`).

- **Punch-through effect treatment:** 2 terms for GSC punch-through jet response deviation between data and MC, one for each detector response simulation method (AF3 and FS).

- **Non-closure**: 1 term applied to AF3 sample to account for the difference between AF3 and FS simulation.

- **High-p_{T} single-particle response**: 1 term for the response to high-p_{T} jets from single-particle and test-beam measurements.

- **b-jets response**: 1 term for the difference between b-jets and light-jets response.

Jet energy resolution

Measurements of JER were performed in bins of p_{T} and η, separately in data using in-situ techniques and in MC simulation using dijet events [77]. This analysis uses the full correlation JER uncertainty scheme provided for Run 2 analysis with 14 total components: 12 for effective NPs and 2 for difference between data and MC, separately for AF3 and FS [77].

71

Jet vertex tagging

The uncertainty associated with JVT is obtained by varying the JVT efficiency SFs within their uncertainty range [112]. This uncertainty accounts for remaining contamination from pile-up jets after applying pile-up suppression and MC generator choice.

Flavor tagging

Calibration SFs for b-tagging efficiencies and c-/light-jets mistagging rates are derived as a function of p_{T} for b-, c-, light-jets and PCBT score. The full set of flavor tagging-related uncertainties was reduced in dimensions by diagonalizing the uncertainty covariance matrix via eigendecomposition [81], resulting in a compact set of orthogonal NPs for this analysis: 85 for b-jets, 56 for c-jets and 42 for light-jets.

7.1.4 Missing transverse energy

Uncertainties on $E_{\mathrm{T}}^{\mathrm{miss}}$ arise from possible mis-calibration of the soft-track component and are estimated using data-to-MC comparison of the p_{T} scale and resolution between the hard and soft $E_{\mathrm{T}}^{\mathrm{miss}}$ components [86]. These uncertainties are represented by three independent terms: 1 for scale uncertainty and 2 for resolution uncertainty of the parallel and perpendicular components.

7.2 Modeling uncertainties

7.2.1 Signal and irreducible background uncertainties

The signal and background samples used were modeled using MC simulation. Most uncertainties on simulation parameters (e.g. generator choice, PS model) are estimated by varying the relevant parameters and comparing them with the nominal sample. Uncertainties involving PDF in particular for most processes in the analysis are set to a flat 1% uncertainty. Cross-section uncertainties were considered for all irreducible background except $t\bar{t}W$. Extra uncertainties for the production of four or more b-jets (additional b-jets) in association with $t\bar{t}X$ and HF jets were also considered due to a lack of theoretical predictions or dedicated measurements, rendering MC modeling challenging. Uncertainties from missing higher-order QCD corrections in MC simulation are estimated by varying the renormalization scale μ_R and factorization scale μ_F within seven different combinations

$$(\mu_R, \mu_F) = \{(0.5, 0.5), (0.5, 1), (1, 0.5), (1, 1), (1, 2), (2, 1), (2, 2)\}.$$

Process-specific uncertainty treatments are detailed below.

SM $t\bar{t}t\bar{t}$ background

The generator uncertainty for SM $t\bar{t}t\bar{t}$ background was evaluated between a nominal sample of MADGRAPH5_AMC@NLO and SHERPA. Parton shower uncertainty was evaluated between PYTHIA8 and HERWIG. The cross-section uncertainty was estimated to be 20% computed from a prediction at NLO in QCD+EW [95].

$t\bar{t}t$ background

The cross-section uncertainty for $t\bar{t}t$ was estimated to be 30% computed from a prediction at NLO in QCD+EW [95]. Events with additional b-jets also incur a 50% uncertainty.

$t\bar{t}W$, $t\bar{t}Z$, $t\bar{t}H$ backgrounds

For $t\bar{t}W$, $t\bar{t}Z$ and $t\bar{t}H$ backgrounds, an uncertainty of 50% is assigned to events with one additional truth b-jets that did not originate from a top quark decay, and an added 50% uncertainty is assigned to events with two or more [113]. The generator uncertainty was estimated for $t\bar{t}Z$ using a MadGraph5_aMC@NLO nominal sample and a Sherpa sample, and for $t\bar{t}H$ using PowhegBox samples interfaced with Pythia8 (nominal) and Herwig7. Cross-section uncertainties of 12% and 10% were applied to $t\bar{t}Z$ and $t\bar{t}H$ respectively [114]. No $t\bar{t}W$ cross-section or PDF uncertainty was considered since the normalizations and jet multiplicity spectrum for $t\bar{t}W$ are estimated using the data-driven method described in section 6.3.3.

Other backgrounds

Other backgrounds include processes with small overall contribution in the SR. The cross-section uncertainty for tZ and tWH is considered to be 30% [115, 116]. A conservative cross-section uncertainty of 50% is applied to $t\bar{t}VV$, VVV and VH. For VV, the cross-section uncertainty is dependent on jet multiplicity and is considered to be 20%/50%/60% for events with $\leq 3/4/\geq 5$ jets [117]. For VV, $t\bar{t}VV$, VVV and VH events with additional truth b-jets, an uncertainty of 50% is applied.

7.2.2 Reducible background uncertainties

Reducible backgrounds consist of $t\bar{t}/V$+HF jets and single top events. Reducible background has small contamination within the SR, thus uncertainties related to reducible background have minor impact. Treatment for reducible background in this analysis largely follows Ref. [10], except for QmisID.

Charge misidentification

Uncertainties on the QmisID background originate from the charge flip rates obtained using the data-driven method described in section 6.3.2. Four sources of uncertainty were considered: statistical uncertainty from the maximum LLH estimation using Equation 6.2; uncertainty from choice of the Z-mass window and sidebands; non-closure uncertainty defined as the relative difference between the number of SS and OS events; and statistical uncertainty from the N_{jets} dependency correction SFs. The combined uncertainties from all four sources are calculated separately for each region involved in section 6.3.2, and are treated as correlated across all regions. Figure 7.1 shows the uncertainty calculated for SR.

Internal (low γ^*) and material conversion

The normalization for internal and material conversion background are free parameters in the fit, as a result the only uncertainties evaluated are from the shape of the distributions used in the template fit method (see section 6.3.1). The uncertainties on internal (material) conversion are estimated based on the difference between data and MC prediction in a region enriched in $Z + \gamma \rightarrow \mu^+\mu^- + e^+e^-$ events.
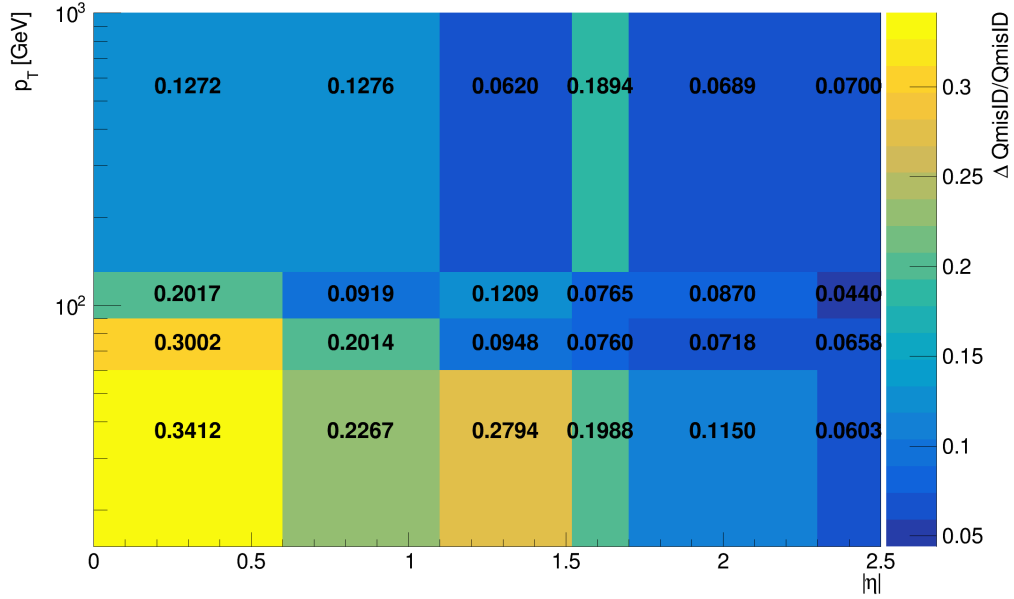
Figure 7.1: Combined QmisID uncertainty rate for SR in bins of $|\eta|$ and p_{T}.

Heavy-flavor non-prompt lepton

Similar to the conversion backgrounds, the uncertainties on non-prompt HF decays come from the shape of the distributions, and are estimated by comparing data and MC prediction between all regions in the analysis on a per bin basis. The events used are required to contain at least one *Loose* reconstructed lepton used in the region selection criteria detailed in Table 6.2 to maintain orthogonality with the SR.

Light-flavor decays and other fake/non-prompt backgrounds

A conservative normalization uncertainty of 100% is assigned for light-flavor non-prompt lepton background [106], and an ad-hoc normalization uncertainty of 30% is applied to all other fake and non-prompt backgrounds. The shape uncertainties for these backgrounds are negligible.

Chapter 8. Results

8.1 Statistical analysis

This section provides an overview of the statistical methods needed to interpret the collected and simulated data to estimate unknown physics parameters and determine compatibility between data and the analysis hypothesis. For the BSM resonance search, the null hypothesis H_0 assumes only SM background contributions and none from any new resonance in the data.

8.1.1 Profile likelihood fit

Given a set of observed data points $\mathbf{x} = [x_1, x_2, \ldots]$ and unknown parameters $\boldsymbol{\theta} = [\theta_1, \theta_2, \ldots, \theta_n]$, the maximum likelihood method aims to find an estimate $\hat{\boldsymbol{\theta}}$ that maximizes the joint probability function $f(\mathbf{x}, \boldsymbol{\theta})$, or in other words the set of parameters that gives the highest probability of observing the collected data points for a particular model. The function to be maximized for this purpose is the log-likelihood (LLH) function $\ln \mathcal{L}(\mathbf{x}, \boldsymbol{\theta})$ where $\mathcal{L}(\mathbf{x}, \boldsymbol{\theta}) \equiv \prod_i f(x_i, \boldsymbol{\theta})$ is defined as the likelihood (LH) function. The LLH is maximized when $\partial/\partial\theta_i (\ln \mathcal{L}) = 0$ for each parameter θ_i.

For an usual binned physics analysis, the above variables for the LH function $\mathcal{L}$ can be expressed as nuisance parameters (NP) $\boldsymbol{\theta}$ and number of events for a model $N_i(\mu)$ for the ith bin, where μ is the targeted parameter of interest (POI). In this analysis, N_i is assumed to follow a Poisson distribution and depends on the following quantities: the signal strength μ defined as the ratio of observed to expected cross sections $\sigma_{\text{obs}}/\sigma_{\text{exp}}$; nuisance parameters $\boldsymbol{\theta}$ which represents the effects of systematic uncertainties, implemented in the

LH function as Gaussian constraints; and normalization factors (NFs) $\boldsymbol{\lambda}$ that control the normalization of background components that do not have a well-known cross section. The Poisson probability of observing exactly N_i events for an expected number of event n_i is

$$\mathcal{P}(N_i|n_i(\mu,\boldsymbol{\lambda})) = \frac{n_i^{N_i}e^{-n_i}}{N_i!}. \tag{8.1}$$

The expected Poisson event number in a bin i can be parameterized as

$$n_i = \mu s_i(\boldsymbol{\theta}) + \sum_j \lambda_j b_{ij}(\boldsymbol{\theta}), \tag{8.2}$$

where s_i is the number of signal events in bin i of every region, and b_{ij} is the number of events for a certain background source index j in bin i. The LH function in this analysis can be written as

$$\mathcal{L}(\mathbf{N}|\mu,\boldsymbol{\theta},\boldsymbol{\lambda}) = \left(\prod_i \mathcal{P}(N_i|n_i)\right) \cdot \prod_k \mathcal{G}(\theta_k), \tag{8.3}$$

where $\mathcal{G}(\theta_k)$ is the Gaussian constraint for a NP k. The signal significance μ and NFs $\boldsymbol{\lambda}$ are left unconstrained and are fitted simultaneously in the profile LH fit. From Neyman-Person lemma citation, the optimal test statistic for hypothesis testing is a function dependent on the profile LH ratio defined as

$$q_\mu \equiv -2\ln\frac{\mathcal{L}(\mu,\hat{\hat{\boldsymbol{\theta}}}_\mu,\hat{\hat{\boldsymbol{\lambda}}}_\mu)}{\mathcal{L}(\hat{\mu},\hat{\boldsymbol{\theta}},\hat{\boldsymbol{\lambda}})}, \tag{8.4}$$

where $\hat{\mu}$, $\hat{\boldsymbol{\theta}}$ and $\hat{\boldsymbol{\lambda}}$ are parameter values that optimally maximizes the LH function, and $\hat{\hat{\boldsymbol{\theta}}}_\mu$, $\hat{\hat{\boldsymbol{\lambda}}}_\mu$ are NP and NF values respectively that maximize the LH function for a given μ.

8.1.2 Exclusion limits

8.2 Fit results

Fit setup

- Plain Asimov fit (only mentioning briefly): all regions included; simulated data used in the fit match exactly to MC prediction with nominal $\mu_{t\bar{t}Z'}$ set to 0 and allowed to free-float.

  Purpose: to perform studies on optimizing fitted parameters and expected sensitivity;refining background estimation techniques; optimizing region definition and object definition

- Real SRs-blinded fit: similar to plain Asimov, but use observed data in CRs.

  Purpose: study the behavior of background estimation using real observed data in CRs on Asimov data in SRs and assessing the influence of statistical effects on fitted parameters and expected sensitivity

- Real SRs-unblinded/H_T fit: all regions included,

Limits

Chapter 9. Summary

References

[1] C. Yang and R. Mills. *Conservation of Isotopic Spin and Isotopic Gauge Invariance.* Phys. Rev. 96 (1 1954), pp. 191–195 (cit. on pp. 1, 10).

[2] A. Milsted and T. J. Osborne. *Quantum Yang-Mills theory: An overview of a program.* Phys. Rev. D 98 (1 2018), p. 014505 (cit. on pp. 1, 10).

[3] P. Higgs. *Broken symmetries and the masses of gauge bosons.* Phys. Rev. Lett. 13 (16 1964), pp. 508–509 (cit. on pp. 1, 14).

[4] P. Higgs. *Broken symmetries, massless particles and gauge fields.* Physics Letters 12.2 (1964), pp. 132–133. ISSN: 0031-9163 (cit. on pp. 1, 14).

[5] F. Englert and R. Brout. *Broken Symmetry and the Mass of Gauge Vector Mesons.* Phys. Rev. Lett. 13 (9 1964), pp. 321–323 (cit. on pp. 1, 14).

[6] ATLAS Collaboration. *Observation of a new particle in the search for the Standard Model Higgs boson with the ATLAS detector at the LHC.* Phys. Lett. B 716 (2012), p. 1. arXiv: 1207.7214 [hep-ex] (cit. on pp. 2, 14).

[7] CMS Collaboration. *Observation of a new boson at a mass of 125 GeV with the CMS experiment at the LHC.* Phys. Lett. B 716 (2012), p. 30. arXiv: 1207.7235 [hep-ex] (cit. on pp. 2, 14).

81

[8] M. Cristinziani and M. Mulders. *Top-quark physics at the Large Hadron Collider.* Journal of Physics G: Nuclear and Particle Physics 44.6 (2017), p. 063001. arXiv: 1606.00327 [hep-ex] (cit. on pp. 2, 8).

[9] ATLAS Collaboration. *Search for top-philic heavy resonances in pp collisions at $\sqrt{s} = 13\,TeV$ with the ATLAS detector.* Eur. Phys. J. C 84 (2024), p. 157. arXiv: 2304.01678 [hep-ex] (cit. on pp. 3, 4, 17).

[10] ATLAS Collaboration. *Observation of four-top-quark production in the multilepton final state with the ATLAS detector.* Eur. Phys. J. C 83 (2023), p. 496. arXiv: 2303.15061 [hep-ex] (cit. on pp. 3, 4, 17, 50, 60, 65, 75).

[11] N. Greiner, K. Kong, J.-C. Park, S. C. Park, and J.-C. Winter. *Model-independent production of a top-philic resonance at the LHC.* Journal of High Energy Physics 2015.4 (2015), p. 29. ISSN: 1029-8479. arXiv: 1410.6099 [hep-ph] (cit. on pp. 3, 18, 19).

[12] ATLAS Collaboration. *Evidence for $t\bar{t}t\bar{t}$ production in the multilepton final state in proton–proton collisions at $\sqrt{s} = 13\,TeV$ with the ATLAS detector.* Eur. Phys. J. C 80 (2020), p. 1085. arXiv: 2007.14858 [hep-ex] (cit. on pp. 4, 65).

[13] D. H. Perkins. *Introduction to High Energy Physics.* 4th. Cambridge, UK: Cambridge University Press, Apr. 2000. ISBN: 9780521621960 (cit. on p. 5).

[14] C. Burgard and D. Galbraith. *Standard Model of Physics.* URL: https://texample. net/model-physics/ (visited on 06/02/2025) (cit. on p. 6).

[15] H. Georgi. *Lie Algebras in Particle Physics: from Isospin to Unified Theories.* 2nd. CRC Press, 2000. ISBN: 9780429499210 (cit. on pp. 7, 10).

[16]   S. Navas et al. *Review of particle physics*. Phys. Rev. D 110.3 (2024), p. 030001 (cit. on p. 8).

[17]   H. de la TorreTrisha Farooque and T. Farooque. *Looking beyond the Standard Model with Third Generation Quarks at the LHC*. Symmetry 14.3 (2022), p. 444 (cit. on p. 8).

[18]   Q.-H. Cao, J.-N. Fu, Y. Liu, X.-H. Wang, and R. Zhang. *Probing Topphilic New Physics via FourTopQuark Production*. Chinese Physics C 45.9 (2021), p. 093107. arXiv: 2105.03372 [hep-ph] (cit. on p. 8).

[19]   H. Beauchesne et al. *A case study about BSM vector resonances with direct couplings to the third quark generation*. European Physical Journal C 80.5 (2020), p. 485. arXiv: 1908.11619 [hep-ph] (cit. on p. 8).

[20]   F. Maltoni, D. Pagani, and S. Tentori. *Topquark pair production as a probe of light topphilic scalars and anomalous Higgs interactions*. Journal of High Energy Physics 2024.9 (Sept. 2024), p. 098. arXiv: 2406.06694 [hep-ph] (cit. on p. 8).

[21]   CMS Collaboration. *Search for $t\bar{t}H$ production in the $H \rightarrow b\bar{b}$ decay channel with leptonic $t\bar{t}$ decays in proton–proton collisions at $\sqrt{s} = 13\,TeV$*. JHEP 03 (2019), p. 026. arXiv: 1804.03682 [hep-ex] (cit. on p. 8).

[22]   M. E. Peskin and D. V. Schroeder. *An Introduction to Quantum Field Theory*. 1st. Reading, MA, USA: AddisonWesley, 1995. ISBN: 978-0-201-50397-5 (cit. on p. 9).

[23]   D. J. Gross. *The role of symmetry in fundamental physics*. Proceedings of the National Academy of Sciences of the United States of America 93.25 (Dec. 1996), pp. 14256–14259 (cit. on p. 9).

[24] A. Pich. *The Standard Model of electroweak interactions. 2004 European School of High-Energy Physics.* Feb. 2005, pp. 1–48. arXiv: hep-ph/0502010 [hep-ex] (cit. on pp. 11–13).

[25] P. Dev and A. Pilaftsis. *High-temperature electroweak symmetry non-restoration from new fermions and implications for baryogenesis.* Journal of High Energy Physics 2020.9 (Sept. 2020), p. 012. arXiv: 2002.05174 [hep-ph] (cit. on p. 13).

[26] J. Riebesell. *Higgs Potential.* URL: https://tikz.net/higgs-potential/ (visited on 07/07/2025) (cit. on p. 15).

[27] J. Goldstone, A. Salam, and S. Weinberg. *Broken Symmetries.* Phys. Rev. 127 (3 1962), pp. 965–970 (cit. on p. 15).

[28] J. Ellis. *Higgs Physics. 2013 European School of High-Energy Physics.* 2015, pp. 117–168. arXiv: 1312.5672 [hep-ph] (cit. on pp. 15, 16).

[29] C. Collaboration. *Search for New Physics in High-Mass Electron-Positron Events in $p\bar{p}$ Collisions at $\sqrt{s} = 1.96$ TeV.* Phys. Rev. Lett. 99 (17 2007), p. 171802. arXiv: 0707.2524 [hep-ex] (cit. on p. 17).

[30] N. Arkani-Hamed, A. G. Cohen, and H. Georgi. *Electroweak symmetry breaking from dimensional deconstruction.* Physics Letters B 513.1-2 (July 2001), pp. 232–240. arXiv: hep-ph/0105239 [hep-ph] (cit. on p. 17).

[31] T. Han, H. E. Logan, B. McElrath, and L.-T. Wang. *Phenomenology of the little Higgs model.* Phys. Rev. D 67 (9 2003), p. 095004. arXiv: hep-ph/0301040 [hep-ph] (cit. on p. 17).

[32] P. Langacker and M. Plümacher. *Flavor changing effects in theories with a heavy Z' boson with family nonuniversal couplings.* Phys. Rev. D 62 (1 2000), p. 013006. arXiv: hep-ph/0001204 [hep-ph] (cit. on p. 17).

[33] P. Langacker. *The Physics of Heavy Z' Gauge Bosons.* Rev. Mod. Phys. 81 (2009), pp. 1199–1228. arXiv: 0801.1345 [hep-ph] (cit. on p. 17).

[34] G. Ferretti and D. Karateev. *Fermionic UV completions of composite Higgs models.* Journal of High Energy Physics 2014.3 (Mar. 2014). ISSN: 1029-8479 (cit. on pp. 17, 19).

[35] L. Vecchi. *A dangerous irrelevant UV-completion of the composite Higgs.* JHEP 02 (2017), p. 094. arXiv: 1506.00623 [hep-ph] (cit. on pp. 17, 19).

[36] K. Agashe, A. Delgado, M. J. May, and R. Sundrum. *RS1, custodial isospin and precision tests.* JHEP 08 (2003), p. 050. arXiv: hep-ph/0308036 [hep-ph] (cit. on p. 17).

[37] K. Agashe, R. Contino, and A. Pomarol. *The Minimal composite Higgs model.* Nucl. Phys. B719 (2005), pp. 165–187. arXiv: hep-ph/0412089 [hep-ph] (cit. on p. 17).

[38] CMS Collaboration. *Observation of four top quark production in protonproton collisions at $\sqrt{s} = 13\,TeV$.* Physics Letters B 847 (2023), p. 138290. arXiv: 2305.13439 [hep-ex] (cit. on p. 17).

[39] J. H. Kim, K. Kong, S. J. Lee, and G. Mohlabeng. *Probing TeV scale top-philic resonances with boosted top-tagging at the high luminosity LHC.* Phys. Rev. D 94 (3 2016), p. 035023. arXiv: 1604.07421 [hep-ph] (cit. on p. 18).

[40] G. C. Branco et al. *Theory and phenomenology of two-Higgs-doublet models*. Phys. Rept. 516 (2012), pp. 1–102. arXiv: 1106.0034 [hep-ph] (cit. on p. 19).

[41] S. Gori, I.-W. Kim, N. R. Shah, and K. M. Zurek. *Closing the wedge: Search strategies for extended Higgs sectors with heavy flavor final states*. Phys. Rev. D 93 (7 2016), p. 075038. URL: https://link.aps.org/doi/10.1103/PhysRevD.93.075038 (cit. on p. 19).

[42] P. S. B. Dev and A. Pilaftsis. *Maximally symmetric two Higgs doublet model with natural Standard Model alignment*. Journal of High Energy Physics 2014.12 (Dec. 2014), p. 024. arXiv: 1408.3405 [hep-ph] (cit. on p. 19).

[43] P. Sabatini. *Evidence for four-top-quarks production with the ATLAS detector at the Large Hadron Collider*. Tech. rep. Geneva: CERN, 2021. URL: https://cds.cern.ch/record/2784150 (cit. on p. 20).

[44] L. Evans and P. Bryant. *LHC Machine*. JINST 3 (2008), S08001 (cit. on p. 21).

[45] ATLAS Collaboration. *The ATLAS Experiment at the CERN Large Hadron Collider*. JINST 3 (2008), S08003 (cit. on pp. 21, 25–31).

[46] CMS Collaboration. *The CMS Experiment at the CERN LHC*. JINST 3 (2008), S08004 (cit. on p. 21).

[47] T. A. Collaboration. *The ALICE experiment at the CERN LHC*. JINST 3 (2008), S08002 (cit. on p. 21).

[48] T. L. Collaboration. *The LHCb Detector at the LHC*. JINST 3 (2008), S08005 (cit. on p. 21).

[49] E. e. a. Gschwendtner. *AWAKE, The Advanced Proton Driven Plasma Wakefield Acceleration Experiment at CERN*. Nuclear Instruments and Methods in Physics Research Section A 829 (2016), pp. 76–82. arXiv: 1512.05498 [physics.acc-ph] (cit. on p. 22).

[50] J. L. Feng, I. Galon, F. Kling, and S. Trojanowski. *ForwArd Search ExpeRiment at the LHC*. Phys. Rev. D 97 (3 2018), p. 035001. arXiv: 1708.09389 [hep-ph] (cit. on p. 22).

[51] T. K. collaboration. *The design, construction, and commissioning of the KATRIN experiment*. Journal of Instrumentation 16.08 (2021), T08015. arXiv: 2103.04755 [physics.ins-det] (cit. on p. 22).

[52] E. Lopienska. *The CERN accelerator complex, layout in 2022*. General Photo. 2022. URL: https://cds.cern.ch/record/2800984 (visited on 07/08/2025) (cit. on p. 22).

[53] High Luminosity LHC Project Organization. *The HL-LHC project*. 2025. URL: https://hilumilhc.web.cern.ch/content/hl-lhc-project (visited on 06/11/2025) (cit. on p. 23).

[54] ATLAS Collaboration. *Performance of the ATLAS detector using first collision data*. JHEP 09 (2010), p. 056. arXiv: 1005.5254 [hep-ex] (cit. on p. 23).

[55] ATLAS Collaboration. *Luminosity determination in pp collisions at $\sqrt{s} = 13\,TeV$ using the ATLAS detector at the LHC*. Eur. Phys. J. C 83 (2023), p. 982. arXiv: 2212.09379 [hep-ex] (cit. on pp. 24, 50, 68).

[56] J. M. Butterworth, G. Dissertori, and G. P. Salam. *Hard Processes in Proton-Proton Collisions at the Large Hadron Collider*. Annu. Rev. Nucl. Part. Sci. 62 (2012), pp. 387–405. arXiv: 1202.0583 [hep-ex] (cit. on p. 24).

[57] J. Campbell, J. Huston, and W. J. Stirling. *Hard interactions of quarks and gluons: a primer for LHC physics.* Reports on Progress in Physics 70.1 (2006), p. 89. arXiv: hep-ph/0611148 [hep-ex] (cit. on p. 24).

[58] ATLAS Collaboration. *Standard Model Summary Plots October 2023.* ATL-PHYS-PUB-2023-039. 2023. URL: https://cds.cern.ch/record/2882448 (cit. on p. 25).

[59] J. Pequenao and P. Schaffner. *How ATLAS detects particles: diagram of particle paths in the detector.* 2013. URL: https://cds.cern.ch/record/1505342 (visited on 07/08/2025) (cit. on p. 26).

[60] J. Pequenao. *Computer generated image of the ATLAS inner detector.* 2008. URL: https://cds.cern.ch/record/1095926 (visited on 07/08/2025) (cit. on p. 27).

[61] J. Pequenao. *Computer Generated image of the ATLAS calorimeter.* 2008. URL: https://cds.cern.ch/record/1095927 (visited on 07/08/2025) (cit. on p. 29).

[62] ATLAS Collaboration. *Operation of the ATLAS trigger system in Run 2.* JINST 15 (2020), P10004. arXiv: 2007.12539 [physics.ins-det] (cit. on pp. 32, 33).

[63] ATLAS Collaboration. *Performance of the ATLAS track reconstruction algorithms in dense environments in LHC Run 2.* Eur. Phys. J. C 77 (2017), p. 673. arXiv: 1704.07983 [hep-ex] (cit. on p. 34).

[64] T. Cornelissen et al. *Concepts, design and implementation of the ATLAS New Tracking (NEWT).* Tech. rep. Geneva: CERN, 2007. URL: https://cds.cern.ch/record/1020106 (cit. on p. 34).

[65] A. Salzburger and on behalf of the ATLAS Collaboration. *Optimisation of the ATLAS Track Reconstruction Software for Run-2.* Journal of Physics: Conference Series 664.7 (2015), p. 072042 (cit. on p. 34).

[66] R. Frühwirth. *Application of Kalman filtering to track and vertex fitting*. Nucl. Instrum. Methods Phys. Res. A 262.2 (1987), pp. 444–450. ISSN: 0168-9002 (cit. on p. 34).

[67] T. Cornelissen et al. *The global χ^2 track fitter in ATLAS*. Journal of Physics: Conference Series 119.3 (2008), p. 032013 (cit. on p. 34).

[68] ATLAS Collaboration. *Improved electron reconstruction in ATLAS using the Gaussian Sum Filter-based model for bremsstrahlung*. ATLAS-CONF-2012-047. 2012. URL: https://cds.cern.ch/record/1449796 (cit. on p. 34).

[69] D. Wicke. *A new algorithm for solving tracking ambiguities*. Tech. rep. Oct. 1998. URL: https://cds.cern.ch/record/2625731 (cit. on p. 35).

[70] ATLAS Collaboration. *Reconstruction of primary vertices at the ATLAS experiment in Run 1 proton–proton collisions at the LHC*. Eur. Phys. J. C 77 (2017), p. 332. arXiv: 1611.10235 [physics.ins-det] (cit. on p. 35).

[71] W. Waltenberger, R. Frühwirth, and P. Vanlaer. *Adaptive vertex fitting*. Journal of Physics G: Nuclear and Particle Physics 34.12 (2007), N343 (cit. on p. 35).

[72] ATLAS Collaboration. *Secondary vertex finding for jet flavour identification with the ATLAS detector*. ATL-PHYS-PUB-2017-011. 2017. URL: https://cds.cern.ch/record/2270366 (cit. on p. 35).

[73] ATLAS Collaboration. *Performance of pile-up mitigation techniques for jets in pp collisions at $\sqrt{s} = 8\,TeV$ using the ATLAS detector*. Eur. Phys. J. C 76 (2016), p. 581. arXiv: 1510.03823 [hep-ex] (cit. on pp. 36, 39).

[74] ATLAS Collaboration. *Topological cell clustering in the ATLAS calorimeters and its performance in LHC Run 1*. Eur. Phys. J. C 77 (2017), p. 490. arXiv: 1603.02934 [hep-ex] (cit. on pp. 36, 37).

[75] ATLAS Collaboration. *Jet reconstruction and performance using particle flow with the ATLAS Detector*. Eur. Phys. J. C 77 (2017), p. 466. arXiv: 1703.10485 [hep-ex] (cit. on p. 38).

[76] M. Cacciari, G. P. Salam, and G. Soyez. *The anti-k_t jet clustering algorithm*. JHEP 04 (2008), p. 063. arXiv: 0802.1189 [hep-ph] (cit. on p. 38).

[77] ATLAS Collaboration. *Jet energy scale and resolution measured in proton–proton collisions at $\sqrt{s} = 13\,TeV$ with the ATLAS detector*. Eur. Phys. J. C 81 (2021), p. 689. arXiv: 2007.02645 [hep-ex] (cit. on pp. 39, 70, 71).

[78] ATLAS Collaboration. *Jet energy scale measurements and their systematic uncertainties in proton–proton collisions at $\sqrt{s} = 13\,TeV$ with the ATLAS detector*. Phys. Rev. D 96 (2017), p. 072002. arXiv: 1703.09665 [hep-ex] (cit. on pp. 39, 70).

[79] ATLAS Collaboration. *Transforming jet flavour tagging at ATLAS*. Tech. rep. Submitted to: Nature Communications. Geneva: CERN, 2025. arXiv: 2505.19689 (cit. on pp. 40–42).

[80] A. Vaswani et al. *Attention Is All You Need*. 2023. arXiv: 1706.03762 [cs.CL] (cit. on p. 40).

[81] ATLAS Collaboration. *Measurements of b-jet tagging efficiency with the ATLAS detector using $t\bar{t}$ events at $\sqrt{s} = 13\,TeV$*. JHEP 08 (2018), p. 089. arXiv: 1805.01845 [hep-ex] (cit. on pp. 42, 72).

[82] ATLAS Collaboration. *Electron reconstruction and identification in the ATLAS experiment using the 2015 and 2016 LHC proton–proton collision data at $\sqrt{s} = 13\,TeV$.* Eur. Phys. J. C 79 (2019), p. 639. arXiv: 1902.04655 [physics.ins-det] (cit. on pp. 43–45).

[83] ATLAS Collaboration. *Electron Identification with a Convolutional Neural Network in the ATLAS Experiment.* ATL-PHYS-PUB-2023-001. 2023. URL: https://cds.cern. ch/record/2850666 (cit. on p. 45).

[84] ATLAS Collaboration. *Muon reconstruction and identification efficiency in ATLAS using the full Run 2 pp collision data set at $\sqrt{s} = 13\,TeV$.* Eur. Phys. J. C 81 (2021), p. 578. arXiv: 2012.00578 [hep-ex] (cit. on pp. 46, 47).

[85] ATLAS Collaboration. *Muon reconstruction performance of the ATLAS detector in proton–proton collision data at $\sqrt{s} = 13\,TeV$.* Eur. Phys. J. C 76 (2016), p. 292. arXiv: 1603.05598 [hep-ex] (cit. on p. 47).

[86] ATLAS Collaboration. *Performance of missing transverse momentum reconstruction with the ATLAS detector using proton–proton collisions at $\sqrt{s} = 13\,TeV$.* Eur. Phys. J. C 78 (2018), p. 903. arXiv: 1802.08168 [hep-ex] (cit. on pp. 48, 72).

[87] ATLAS Collaboration. *E_T^{miss} performance in the ATLAS detector using 2015–2016 LHC pp collisions.* ATLAS-CONF-2018-023. 2018. URL: https://cds.cern.ch/record/ 2625233 (cit. on p. 49).

[88] J. Alwall et al. *The automated computation of tree-level and next-to-leading order differential cross sections, and their matching to parton shower simulations.* JHEP 07 (2014), p. 079. arXiv: 1405.0301 [hep-ph] (cit. on pp. 51, 53, 54).

[89] NNPDF Collaboration, R. D. Ball, et al. *Parton distributions for the LHC run II.* JHEP 04 (2015), p. 040. arXiv: 1410.8849 [hep-ph] (cit. on pp. 51, 53, 54).

[90] T. Sjöstrand et al. *An introduction to PYTHIA 8.2.* Comput. Phys. Commun. 191 (2015), p. 159. arXiv: 1410.3012 [hep-ph] (cit. on pp. 51, 53, 54).

[91] ATLAS Collaboration. *ATLAS Pythia 8 tunes to 7 TeV data.* ATL-PHYS-PUB-2014-021. 2014. URL: https://cds.cern.ch/record/1966419 (cit. on pp. 53, 54).

[92] S. Frixione, E. Laenen, P. Motylinski, and B. R. Webber. *Angular correlations of lepton pairs from vector boson and top quark decays in Monte Carlo simulations.* JHEP 04 (2007), p. 081. arXiv: hep-ph/0702198 (cit. on p. 53).

[93] P. Artoisenet, R. Frederix, O. Mattelaer, and R. Rietkerk. *Automatic spin-entangled decays of heavy resonances in Monte Carlo simulations.* JHEP 03 (2013), p. 015. arXiv: 1212.3460 [hep-ph] (cit. on p. 53).

[94] D. J. Lange. *The EvtGen particle decay simulation package.* Nucl. Instrum. Meth. A 462 (2001), p. 152 (cit. on p. 53).

[95] R. Frederix, D. Pagani, and M. Zaro. *Large NLO corrections in $t\bar{t}W^{\pm}$ and $t\bar{t}t\bar{t}$ hadroproduction from supposedly subleading EW contributions.* JHEP 02 (2018), p. 031. arXiv: 1711.02116 [hep-ph] (cit. on pp. 53, 73, 74).

[96] E. Bothmann et al. *Event generation with Sherpa 2.2.* SciPost Phys. 7.3 (2019), p. 034. arXiv: 1905.09127 [hep-ph] (cit. on pp. 53, 54).

[97] S. Schumann and F. Krauss. *A parton shower algorithm based on Catani–Seymour dipole factorisation.* JHEP 03 (2008), p. 038. arXiv: 0709.1027 [hep-ph] (cit. on p. 53).

[98] S. Höche, F. Krauss, M. Schönherr, and F. Siegert. *A critical appraisal of NLO+PS matching methods*. JHEP 09 (2012), p. 049. arXiv: 1111.1220 `[hep-ph]` (cit. on p. 53).

[99] S. Höche, F. Krauss, M. Schönherr, and F. Siegert. *QCD matrix elements + parton showers. The NLO case*. JHEP 04 (2013), p. 027. arXiv: 1207.5030 `[hep-ph]` (cit. on p. 53).

[100] S. Catani, F. Krauss, B. R. Webber, and R. Kuhn. *QCD Matrix Elements + Parton Showers*. JHEP 11 (2001), p. 063. arXiv: hep-ph/0109231 (cit. on p. 53).

[101] S. Höche, F. Krauss, S. Schumann, and F. Siegert. *QCD matrix elements and truncated showers*. JHEP 05 (2009), p. 053. arXiv: 0903.1219 `[hep-ph]` (cit. on p. 53).

[102] F. Cascioli, P. Maierhöfer, and S. Pozzorini. *Scattering Amplitudes with Open Loops*. Phys. Rev. Lett. 108 (2012), p. 111601. arXiv: 1111.5206 `[hep-ph]` (cit. on p. 53).

[103] A. Denner, S. Dittmaier, and L. Hofer. COLLIER*: A fortran-based complex one-loop library in extended regularizations*. Comput. Phys. Commun. 212 (2017), pp. 220–238. arXiv: 1604.06792 `[hep-ph]` (cit. on p. 53).

[104] F. Buccioni et al. *OpenLoops 2*. Eur. Phys. J. C 79.10 (2019), p. 866. arXiv: 1907.13071 `[hep-ph]` (cit. on p. 53).

[105] ATLAS Collaboration. *ATLAS data quality operations and performance for 2015–2018 data-taking*. JINST 15 (2020), P04003. arXiv: 1911.04632 `[physics.ins-det]` (cit. on p. 55).

[106] ATLAS Collaboration. *Analysis of $t\bar{t}H$ and $t\bar{t}W$ production in multilepton final states with the ATLAS detector*. ATLAS-CONF-2019-045. 2019. URL: https://cds.cern.ch/record/2693930 (cit. on pp. 60, 63, 76).

[107] ATLAS Collaboration. *Measurement of the total and differential cross-sections of $t\bar{t}W$ production in pp collisions at $\sqrt{s} = 13\,TeV$ with the ATLAS detector.* JHEP 05 (2024), p. 131. arXiv: 2401.05299 [hep-ex] (cit. on p. 60).

[108] ATLAS Collaboration. *Search for new phenomena in events with same-charge leptons and b-jets in pp collisions at $\sqrt{s} = 13\,TeV$ with the ATLAS detector.* JHEP 12 (2018), p. 039. arXiv: 1807.11883 [hep-ex] (cit. on p. 63).

[109] ATLAS Collaboration. *Search for R-parity-violating supersymmetry in a final state containing leptons and many jets with the ATLAS experiment using $\sqrt{s} = 13\,TeV$ proton–proton collision data.* Eur. Phys. J. C 81 (2021), p. 1023. arXiv: 2106.09609 [hep-ex] (cit. on p. 65).

[110] E. Gerwick, T. Plehn, S. Schumann, and P. Schichtel. *Scaling Patterns for QCD Jets.* JHEP 10 (2012), p. 162. arXiv: 1208.3676 [hep-ph] (cit. on p. 66).

[111] G. Avoni et al. *The new LUCID-2 detector for luminosity measurement and monitoring in ATLAS.* JINST 13.07 (2018), P07017 (cit. on p. 68).

[112] ATLAS Collaboration. *Tagging and suppression of pileup jets.* ATL-PHYS-PUB-2014-001. 2014. URL: https://cds.cern.ch/record/1643929 (cit. on pp. 70, 72).

[113] ATLAS Collaboration. *Measurements of inclusive and differential fiducial cross-sections of $t\bar{t}$ production with additional heavy-flavour jets in proton–proton collisions at $\sqrt{s} = 13\,TeV$ with the ATLAS detector.* JHEP 04 (2019), p. 046. arXiv: 1811.12113 [hep-ex] (cit. on p. 74).

[114] D. de Florian et al. *Handbook of LHC Higgs Cross Sections: 4. Deciphering the Nature of the Higgs Sector.* CERN Yellow Rep. Monogr. 2 (2017), pp. 1–869. arXiv: 1610.07922 [hep-ph] (cit. on p. 74).

[1844] [115] ATLAS Collaboration. *Measurement of the production cross-section of a single top quark in association with a Z boson in proton–proton collisions at* 13 *TeV with the ATLAS detector*. ATLAS-CONF-2017-052. 2017. URL: https://cds.cern.ch/record/2273868 (cit. on p. 74).

[1848] [116] F. Demartin, B. Maier, F. Maltoni, K. Mawatari, and M. Zaro. *tWH associated production at the LHC*. EPJC 77.1 (2017). arXiv: 1607.05862 [hep-ph]. URL: https://doi.org/10.1140/epjc/s10052-017-4601-7 (cit. on p. 74).

[1851] [117] ATLAS Collaboration. *Measurement of $W^{\pm}Z$ production cross sections and gauge boson polarisation in pp collisions at $\sqrt{s} = 13$ TeV with the ATLAS detector*. Eur. Phys. J. C 79 (2019), p. 535. arXiv: 1902.05759 [hep-ex] (cit. on p. 74).